

1 **Use of Multivariate Analysis for Synchrotron Micro-XANES Analysis of Iron**
2 **Valence State in Amphiboles**

3
4 **M. DARBY DYAR¹, ELLY A. BREVES¹, MICKEY E. GUNTER², ANTONIO LANZIROTTI³,**
5 **JONATHAN M. TUCKER⁴, CJ CAREY⁵, SAMANTHA E. PEEL⁶, ELIZABETH B. BROWN¹, ROBERTA**
6 **OBERTI⁷, MIRNA LEROTIC⁸, AND JEREMY S. DELANEY⁹**

7
8 ¹Department of Astronomy, Mount Holyoke College, South Hadley, MA 01075, U.S.A.

9 ²Department of Geological Sciences, University of Idaho, Moscow, ID 83844, U.S.A.

10 ³Center for Advanced Radiation Sources, University of Chicago, 5640 S. Ellis Ave., Chicago, IL
11 60637, U.S.A.

12 ⁴Department of Earth and Planetary Science, Harvard University, 20 Oxford Street, Cambridge,
13 MA 02138, U.S.A.

14 ⁵School of Computer Sciences, University of Massachusetts at Amherst, Amherst, MA 01003,
15 U.S.A.

16 ⁶Department of Earth and Planetary Sciences, The University of Tennessee, 1412 Circle Dr.,
17 Knoxville, TN 37996, U.S.A.

18 ⁷CNR-Istituto di Geoscienze e Georisorse, Unità di Pavia, via Ferrata, 1 I-27100 Pavia, Italy

19 ⁸2nd Look Consulting, 1702 17/F Tung Hip Commercial Building, 248 Des Voeux Road, Hong Kong

20 ⁹Department of Earth and Planetary Sciences, Rutgers University, Piscataway, NJ 08854, U.S.A.

21
22 **REVISION #1**

23 Keywords: amphibole, x-ray absorption spectroscopy, x-ray near-edge spectroscopy, kaersutite,
24 potassic-magnesio-hastingsite, oxo-potassic-magnesio-hastingsite, pargasite, magnesio-
25 hornblende, actinolite, magnesio-edenite, partial least-squares analysis, lasso, garnet

26

ABSTRACT

27

Microanalysis of $\text{Fe}^{3+}/\Sigma\text{Fe}$ in geological samples using synchrotron-based X-ray

28

absorption spectroscopy has become routine since the introduction of standards and model

29

compounds. Existing calibrations commonly use least squares linear combinations of pre-edge

30

and edge data from standard reference spectra with known coordination number and valence

31

state acquired on powdered samples to avoid preferred orientation. However, application of these

32

methods to single mineral grains is appropriate only for isometric minerals and limits their

33

application to analysis of *in situ* grains in thin sections. In this work, a calibration suite

34

developed by acquiring X-ray absorption near-edge spectroscopy (XANES) data from amphibole

35

single crystals with the beam polarized along the major optical directions (X, Y, and Z) is

36

employed. Seven different methods for predicting $\% \text{Fe}^{3+}$ were employed based on 1) area-

37

normalized pre-edge peak centroid, 2) the energy of the main absorption edge at the location

38

where the normalized edge intensity has the highest R^2 correlation with $\text{Fe}^{3+}/\Sigma\text{Fe}$, 3) the ratio of

39

spectral intensities at two energies determined by highest R^2 correlation with $\text{Fe}^{3+}/\Sigma\text{Fe}$, 4) use of

40

the slope (first derivative) at every channel to select the best predictor channel, 5,6) partial least-

41

squares models with variable and constant numbers of components, and 7) least absolute

42

shrinkage and selection operator models. The latter three sophisticated multivariate analysis

43

techniques for predicting $\text{Fe}^{3+}/\Sigma\text{Fe}$ show significant improvements in accuracy over the former

44

four types of univariate models. $\text{Fe}^{3+}/\Sigma\text{Fe}$ can be measured in randomly-oriented amphibole

45

single crystals with an accuracy of ± 5.5 - 6.2% absolute. Multivariate approaches demonstrate that

46

for amphiboles main edge and EXAFS regions contain important features for predicting valence

47

state. This suggests that in this mineral group, local structural changes accommodating site

- 48 occupancy by Fe^{3+} vs. Fe^{2+} have a pronounced (and diagnostic) effect on the XAS spectra that
- 49 can be reliably used to precisely constrain $\text{Fe}^{3+}/\Sigma\text{Fe}$.

50

INTRODUCTION

51 A growing worldwide community of synchrotron users is pursuing studies of the redox
52 state of iron at microscales within minerals and glasses using Fe K-edge X-ray absorption near-
53 edge structure (XANES) spectroscopy. For these materials, there is a general consensus that
54 calibrations based on the intensity and energy of the Fe K-edge pre-edge signal, which is
55 composed of contributions from Fe cations in different valence states and coordination
56 polyhedra, provides a fairly representative measure of Fe valence state. The area-weighted
57 average peak centroid energy of the pre-edge multiplets has been shown to be representative of
58 contributions from the composite transitions, as first pioneered by Bajt et al. (1994).
59 Subsequently it was recognized that the intensity of the pre-edge signal is also a function of site
60 distortion and coordination, so Galois et al. (2001) utilized pseudo-Voigt line shapes of
61 minerals with known coordination geometries to deconvolute XANES pre-edge spectra into
62 component peaks, e.g., andradite spectra are used for $^{[6]}\text{Fe}^{3+}$, augite glass for $^{[4,5]}\text{Fe}^{2+}$, berlinite
63 for $^{[4]}\text{Fe}^{3+}$, staurolite for $^{[4]}\text{Fe}^{2+}$, and siderite for $^{[6]}\text{Fe}^{2+}$. This work was generalized by Wilke et al.
64 (2001) and Petit et al. (2001), who characterized and fit 30 minerals and synthetic compounds to
65 correlate energy and intensity of pre-edge features with oxidation state and local coordination
66 environments. The Wilke et al. (2001) calibration has been used often to predict Fe^{3+} and Fe^{2+}
67 contents in geological materials, but it is inherently limited by its requisite use on powders and
68 the known differences in site geometry between their reference materials and the unknown
69 minerals.

70 For petrologic applications, the true “Holy Grail” for microanalysis of $\text{Fe}^{3+}/\Sigma\text{Fe}$ is *in situ*
71 microanalysis of individual mineral grains in thin sections which preserves the petrological
72 relationship between mineral grains in the section, an endeavor complicated by anisotropy of

73 most common rock-forming minerals. To test the effects of orientation, Dyar et al. (2002a,b)
74 aligned the vibration direction of the polarized synchrotron beam along the major optical
75 directions (X, Y, and Z) of single crystals of biopyriboles, olivine, scapolite, and feldspar. Their
76 results show significant variation over the entire XANES energy range (pre-edge and main-edge)
77 that propagates 10-20% absolute errors on measurements of %Fe³⁺ using pre-edge-based
78 techniques for quantification. It is apparent from this work and that of others (Dräger et al. 1988,
79 Scordari et al. 2010, Mino et al. 2014, Evans et al. 2014) that useful predictions of Fe³⁺/ΣFe in
80 single crystals must consider the full range of possible optical orientations in order to encompass
81 all possible electronic transitions in each mineral of interest. This process should be
82 fundamentally analogous to determinations of species abundances based on spectral features in
83 the visible and infrared wavelengths.

84 In this paper, we focus on the amphibole mineral group, which has a range of four
85 possible [6] or [6+2] coordinated polyhedra that can be occupied by Fe³⁺ and Fe²⁺. We use a
86 suite of samples characterized both chemically and by single-crystal X-ray diffraction to relate
87 peak energies and intensities directly to the geometry of the *M*(1)-*M*(4) sites. We use spectra
88 acquired with the crystals oriented such that the polarization direction of the synchrotron beam is
89 parallel to their X, Y, and Z optical orientation directions, choosing samples that cover a range of
90 composition and extremes of Fe³⁺/ΣFe, enabled in part by thermal heating and resultant
91 oxidation of a subset of samples. We extract the pre-edge region of the XANES spectra to fit
92 component peaks representing contributions from both Fe²⁺ and Fe³⁺ in this region, and compare
93 those peaks to known Fe³⁺/ΣFe from bulk methods. We also examine R² correlation of three
94 derived spectral features (normalized intensity in the main edge, intensity ratios, and slope) with
95 Fe³⁺/ΣFe to select the channels best used for univariate prediction of Fe³⁺/ΣFe. Finally, we use

96 multivariate analysis techniques and the spectra from the entire XANES region to predict
97 $\text{Fe}^{3+}/\Sigma\text{Fe}$, providing a dramatic improvement over the accuracy of univariate methods. This work
98 establishes a protocol for XANES analysis of other anisotropic mineral groups, and lays the
99 groundwork for producing precise and accurate routine XANES analyses of $\text{Fe}^{3+}/\Sigma\text{Fe}$ in
100 randomly-oriented grains in thin sections using partial least squares (PLS) and least absolute
101 shrinkage and selection operator (lasso) regression.

102 **BACKGROUND**

103 Bajt et al. (1994) were the first to suggest that a calibration curve for quantitative
104 prediction of $\text{Fe}^{3+}/\Sigma\text{Fe}$ in minerals could be established using the area-weighted centroid energy
105 of the composite pre-edge in three standards: olivine (0% Fe^{3+}), magnetite (67% Fe^{3+}), and
106 hematite (100% Fe^{3+}). Delaney et al. (1998) soon thereafter pointed out that olivine, pyroxene,
107 amphibole, mica, and tourmaline groups each required independent calibration curves due to the
108 differences in coordination polyhedra among them. Galois et al. (2001), Wilke et al. (2001), and
109 Petit et al. (2001) chose a different, more generalized approach using representative minerals
110 from several different groups as model compounds for Fe^{2+} and Fe^{3+} in a variety of site
111 geometries and coordination polyhedra. Wilke et al. (2001) noted that the area-weighted
112 composite pre-edge position varies non-linearly with oxidation state. Their results show a
113 calibration curve similar to that of Bajt et al. (1994) though customized to distinguish between
114 $^{[4]}\text{Fe}^{2+}$, $^{[6]}\text{Fe}^{2+}$, $^{[4]}\text{Fe}^{3+}$, and $^{[6]}\text{Fe}^{3+}$. Many hundreds of workers (e.g., Giuli et al. 2003, 2005,
115 Schmid et al. 2003, Grossemy et al. 2007, Beck et al. 2012, Bonadiman et al. 2014, Debret et al.
116 2014) have subsequently used the generalized Figure 6 from the Wilke et al. (2001) paper to
117 determine redox ratios in a variety of silicate minerals and glasses.

118 However, there are issues with such a generalized technique, acknowledged by Wilke et
119 al. (2001) to have $\pm 10\%$ (absolute) errors on $\text{Fe}^{3+}/\Sigma\text{Fe}$. It applies only to finely ground powders
120 that are effectively isotropic with no preferred orientation. Deviations from their calibration are
121 attributed to the method for numerically extracting the pre-edge from the main edge, and to
122 differences in site geometry between their references and the unknown minerals. Because the $1s$
123 $\rightarrow 3d$ transition is also sensitive to $3d + 4p$ orbital mixing, the intensity of the pre-edge peaks
124 (and thus their calculated areas) is sensitive to site geometry. Pre-edge peak intensities will
125 increase progressively with site distortion from centrosymmetric. The calibration lines are not
126 necessarily linear (Delaney et al., 1996). Wilke et al. (2001) weight the calibration line toward
127 whichever Fe atom is in a more distorted site, and use exclusively the pre-edge region, ignoring
128 potentially significant features associated with the rising-edge and white line ($1s \rightarrow 4s$ and $1s \rightarrow$
129 $4p$ transitions) and Extended X-ray Absorption Fine Structure (EXAFS) regions ($1s$ to
130 continuum) of the spectra. Mixtures of Fe in different sites tend to average out in the Wilke
131 method (Forder et al. 2009) making some solutions non-unique.

132 The intervening decade since this work was done has seen the widespread introduction of
133 high-resolution monochromators that offer the capability to better resolve within the Fe K edge
134 spectra the individual features associated with each type of coordination polyhedron and valence
135 state. An area-weighted approach like that of Wilke et al. (2001) is sensitive to differences in
136 energy resolution of the beamlines used, the particular fitting model used to fit each multiplet
137 peak in the pre-edge and the choice of baseline fit beneath the peaks. All impact the relative area
138 of measured peaks and thus leads to small inconsistencies in calculated area-weighted centroids
139 between research groups and facilities, particularly for highly oxidized or reduced species where

140 the tail of the main edge absorption feature can be difficult to deconvolute accurately. There is a
141 need for alternative approaches.

142 Although the XANES technique works well for isotropic and powdered materials
143 generally irrespective of orientation during analysis, in anisotropic minerals the high degree of
144 linear polarization of the X-ray beam within the orbital plane of the synchrotron storage ring
145 results in variations in XANES spectral intensities as a consequence of X-ray pleochroism. One
146 of the original papers to address this was Dräger et al. (1988), who used thin plates cut from
147 oriented single crystals. They confirmed that isometric samples show identical spectra when the
148 polarization direction is either parallel or perpendicular to an oriented crystal. They observed a
149 conspicuous angular dependence of pre-edge absorption in the anisotropic (hexagonal) minerals
150 hematite and siderite. In hematite, for example, the intensity of a pre-edge peak at 7114 eV is
151 twice as intense with the beam polarization parallel to (001) than it is perpendicular to (001).
152 Delaney et al. (2001), Dyar et al. (2002a,b), Scordari et al. (2010) and Mino et al. (2014)
153 observed similar phenomenon in other oriented mineral samples.

154 Subsequent studies documented the differential interactions of the linearly polarized X-
155 ray beam with anisotropic crystals. Orientation effects were first recognized and extensively
156 characterized in sheet silicates (Manceau et al. 1998, Giuli et al. 2001, Dyar et al. 2001, Mino et
157 al. 2014, Evans et al. 2014). For example, Munoz et al. (2013) applied the magic angle geometry
158 for measurement of Fe-K XANES and pre-edges of phyllosilicates. The “magic tilt angle” for
159 incident X-rays is the angle at which orientation dependent terms vanish from resonant intensity
160 terms (Pettifer et al. 1990, Stöhr 1992). It theoretically reflects the relatively high rotational
161 symmetry of the mica lattice in the basal plane, and provides a fundamental starting point for the
162 determination of the magnitude of angle dependent intensity for oriented slices such as those in

163 thin section (Brouder 1990). However, no magic angle spectra acquired at a constant
164 crystallographic orientation can represent all potential electronic transitions at all
165 crystallographic orientations.

166 The only way to ensure that all possible transitions are represented in crystalline
167 standards is to acquire XANES spectra with the vibration direction of the synchrotron beam
168 parallel to the known optical orientations of each single crystal. We use optical (rather than
169 crystallographic) orientations for two reasons: 1) this is the historical convention for acquisition
170 of visible and infrared spectra, and 2) future users of our techniques could use observable optical
171 directions in a thin section to aid in data collection. We note, however, that in future studies we
172 plan to collect data along both the optical, as well as crystallographic directions when they differ,
173 as occurs for monoclinic amphiboles.

174 The measurements are extremely challenging because they require that crystals be
175 mounted on fibers in goniometer heads and be oriented either through X-ray diffraction or
176 spindle stage microscopy to determine the proper orientations of the crystals on the X-ray
177 absorption (XAS) beamlines. For this reason, there are only a handful of data where spectra were
178 truly acquired along the optical directions X, Y, and Z. Dyar et al. (2002a,b) studied oriented
179 crystals of orthopyroxene (opx), clinopyroxene (cpx), amphibole, biotite, and muscovite. Spectra
180 acquired along the length of the chains (*c* for px, *c* for amph, and *a* for sheet silicates) are similar,
181 with corresponding changes in the optical directions, such that $Y_{\text{musc}} \approx Z_{\text{bt}} \approx Z_{\text{amph}} \approx Z_{\text{opx}} \approx$
182 X_{aegirine} (cpx is intermediate). Spectra taken along the *b* crystallographic axes (along the
183 octahedral layer, across the I-beam) are similar for all groups ($Z_{\text{musc}} \approx Y_{\text{bt}} \approx Y_{\text{amph}} \approx X_{\text{opx}} \approx Y_{\text{cpx}}$),
184 and more similar for the amphiboles and micas. Finally, spectra acquired along the stacking
185 direction, which is the *a* crystallographic direction for pyroxene and amphiboles and the *c*

186 crystallographic direction in sheet silicates, are analogous. From these relationships, and from
187 hints of fundamental peaks within the pre-edge envelopes, it became clear that higher resolution
188 data on pre-edge spectra of oriented samples could potentially elucidate transitions specific to
189 different optical orientations, with energies that can be related to their crystal structures.
190 Moreover, this work demonstrated quantitatively that the effect of orientation on calculated
191 $\text{Fe}^{3+}/\Sigma\text{Fe}$ generates $\pm 10\text{-}20\%$ errors in randomly-oriented crystals using the position of the area-
192 weighted centroid of the pre-edge peaks.

193 The sensitivity of Fe K pre-edges region to valence state reflects the sensitivity of these
194 electronic transitions to valence states of the excited atom. However, other parts of the XANES
195 and EXAFS regions of the absorption spectra also reflect changes that arise from permutations to
196 the local structure around the Fe cations due to the difference in size and charge between Fe^{2+}
197 and Fe^{3+} (Marcus et al. 2008), though the magnitude of such changes will be highly dependent
198 on the specific phase and structure. It stands to reason that an alternative and perhaps more
199 sensitive method for predicting valence state from XAS of any material would be one that
200 utilizes information not only in the pre-edge region, but also extending into the EXAFS energies.

201 For example, Berry et al. (2010) suggest several empirical alternative approaches to
202 calibration of garnet XANES spectra. They report that the average centroid energy of garnet pre-
203 edges is relatively insensitive to $\text{Fe}^{3+}/\Sigma\text{Fe}$, and propose two alternative methods of prediction.
204 The first is to use the absorption edge energy at an arbitrary normalized intensity value of 0.9,
205 though a small offset in the resultant calibration plot is caused by varying size and geometry of
206 the average coordination polyhedra (which are a function of composition) and may diminish its
207 effectiveness. As an alternative, Berry et al. (2010) used information in the main-edge XANES
208 and near-EXAFS regions of their spectra to demonstrate that the ratio of spectral intensities at

209 7138.4 and 7161.7 eV was an accurate predictor of $\text{Fe}^{3+}/\Sigma\text{Fe}$ in mantle garnets. This technique
210 shows great promise, but its choice of which channels to use in predictions is somewhat *ad hoc*
211 and subjective. Moreover, it relies on prior knowledge based on wet chemical or Mossbauer
212 analysis on a painstakingly acquired or synthesized set of matrix-matched mineral standards.

213 Dyar et al. (2012) instead used a multivariate analysis method (partial least squares
214 regression, or PLS) to examine use of full XANES spectra in predicting $\text{Fe}^{3+}/\Sigma\text{Fe}$ in garnets.
215 Previously-proposed techniques for using simple linear regression methods to predict $\text{Fe}^{3+}/\Sigma\text{Fe}$
216 (including those of Berry et al. 2010) were evaluated, along with PLS. Results showed that PLS
217 analysis of the entire XANES spectral region yields significantly better predictions of Fe^{3+} in
218 garnets, with both robustness and generalizability, than approaches based solely on pre-edges.
219 Moreover, their PLS coefficients and loadings clearly demonstrate that the vast majority of the
220 useful information in the XANES spectra for predicting $\text{Fe}^{3+}/\Sigma\text{Fe}$ in garnets is found in the main
221 edge and at higher energies. This result emphasizes that in garnet changes in local coordination
222 and nearest neighbors, which are manifest in the EXAFS region, in part reflect valence state
223 differences. Expanding such calibrations to a wider range of mineral structure types may
224 dramatically improve the accuracy of redox predictions in glasses and minerals. The current
225 paper and work on silicate glasses (Dyar et al., 2014 and submitted) demonstrate such a potential
226 approach where multivariate analysis of the entire XAS region provides $\text{Fe}^{3+}/\Sigma\text{Fe}$ values that are
227 more consistent with values measured using Mössbauer in non-isometric materials such as the
228 amphiboles described here.

229 **SAMPLES STUDIED**

230 Provenance and references to localities from which amphiboles were obtained for this
231 study are listed in Table 1, and their compositions and crystal-chemical formulae in Table 2. All

232 samples were analyzed not only for major elements by electron microprobe, but also for
233 $\text{Fe}^{3+}/\Sigma\text{Fe}$ by Mössbauer (see Dyar et al. 1993 and Oberti et al. 2012) and H_2O by one of two
234 techniques. The bulk technique of uranium extraction was used for the majority of samples
235 studied; it determines H_2O contents by means of a procedure for collecting and measuring all the
236 structural H using a volumetric measurement of water vapor extracted from silicates (see
237 Bigeleisen et al. 1952 and Holdaway et al. 1986 for details of the technique). Samples DL-5, Fr-
238 12, and Z2124 were analyzed for H by secondary ion mass spectrometry (SIMS), based on very
239 careful single-crystal structure refinement (SREF) calibrations that take into account the Fe/Mg
240 ratio (one of the main factors affecting ion yield in amphiboles). More details on the procedures
241 are reported in Ottolini et al. (1995), Ottolini and Oberti (2000) and Oberti et al. (2007).

242 Single crystal x-ray diffraction was used to characterize site occupancies and crystal
243 structures of seven of the samples studied here. Previous high temperature studies on amphibole
244 single crystals (Oberti et al. 2010, 2013) had shown that thermal annealing in un-buffered sealed
245 vials induces Fe oxidation and deprotonation, and that these processes can be monitored
246 accurately by single-crystal X-ray diffraction. In particular, the results of the structure
247 refinements done at different temperatures were interpreted in the light of the experience
248 developed at CNR-IGG Pavia, and allowed precise determination of the site populations and thus
249 of the crystal-chemical formulae. Full details of the structure refinements will be given in a series
250 of papers focussed on thermal expansion and deprotonation in monoclinic calcium and sodium-
251 calcium amphiboles (Oberti et al. 2016, in preparation).

252 For this work, two kaersutites, one potassic-magnesio-hastingsite, and one pargasite
253 samples were selected (Fr-12, DL-5, KAR, and Z2124) and studied both as crystallized in nature
254 and after being heat treated in air at 900°C for 20 hours. In this way, we could obtain samples

255 with the same overall composition but with different cation ordering and values of the $\text{Fe}^{3+}/\text{Fe}^{2+}$
256 ratios. The response of each sample to annealing depends on the amount of the Fe^{2+} content. For
257 kaersutite Fr-12 (0.05 Fe^{2+} *apfu*), only minimal oxidation change could be observed, and hence
258 this sample was examined here only as untreated. In kaersutite DL-5, the Fe^{2+} content (1.14 *apfu*)
259 is high enough to allow complete dehydrogenation under the above conditions for thermal
260 annealing and to maintain a low but significant amount of Fe^{2+} (0.16 *apfu*). In contrast, the
261 potassic-magnesio-hastingsite KAR did not have sufficient Fe^{2+} to allow complete
262 dehydrogenation; thus all Fe was oxidized but residual H remained also after thermal annealing.
263 In pargasite Z2124, the low Fe^{2+} content (0.29 *apfu*) allowed only the same amount of H loss. It
264 is also important to note that significant amounts of cation exchange were observed in samples
265 DL-5 and Z2124, where all $^{\text{B}}\text{Fe}^{2+}$ (at the *M*(4) site) exchanged with $^{\text{C}}\text{Mg}$ (occurring at the *M*(1)
266 and *M*(3) sites, which are both coordinated with the OH groups). All these processes were
267 assessed by structure refinement and crystal chemical analyses of the same crystals which were
268 later oriented and used for XANES analyses.

269 METHODS

270 Experimental methods

271 In preparation for each beam session, single crystals were oriented optically using a
272 polarizing light microscope with a spindle stage. Each crystal was mounted with the *Z* optical
273 orientation parallel to the rotation axis of a spindle stage, permitting acquisition of polarized
274 XANES spectra perpendicular to the double chains (the *a sin β* direction) or within them (either
275 the *b* or *c* crystallographic axes). Ten samples were analyzed in known orientations to the
276 incident beam and 14 samples were analyzed with unknown, random orientation to the incident
277 beam. XANES measurements used a special beam geometry described in Dyar et al. (2002b).

278 Samples were analyzed over the course of three sessions at beamline X26A at the
279 National Synchrotron Light Source (NSLS) at Brookhaven National Laboratory in Upton, NY.
280 Using mutually-orthogonal Kirkpatrick-Baez mirrors, the beam was focused to a $\sim 7 \times 9$ μm area.
281 Incident beam energy was controlled by a water-cooled (9°C) Si(311) channel-cut
282 monochromator. The structure of the Fe K absorption edge was scanned in the near-edge region
283 from 7020-7220 eV. XANES spectra were collected in fluorescence mode using Si drift diode
284 detectors. Acquisition parameters varied between sessions, but all spectra were acquired at a
285 sampling resolution of at least 5.0 eV from 7020-7105 eV, 0.1 eV from 7105-7118 eV, 0.5 eV
286 from 7118-7140 eV, and 1.0 eV from 7140-7220 eV. Because prevailing theory at the time these
287 measurements were made suggested that Fe redox state is primarily evidenced in the pre-edge
288 region, these scans favored 7105-7140 eV in time and energy resolution. The scans were carried
289 out to a maximum energy of 7220 eV to include most significant post-edge oscillations in the
290 absorption spectra to achieve reasonable edge-step normalization.

291 Monochromator energy drift, primarily caused by changing thermal expansion of the
292 silicon monochromator correlated to decrease in storage ring current at the NSLS over time, was
293 monitored with a National Museum of Natural History (NMNH) magnetite standard, and was
294 always analyzed before and after every 2-3 samples from 1995-the present. An energy offset was
295 determined using repeated measurements of the observed pre-edge centroid of the NMNH
296 magnetite standard relative to a reference energy of 7113.25 eV (cf. Westre et al. 1997). Drift of
297 up to 0.6 eV over the NSLS injection cycle, measured by successive magnetite analyses, was
298 modeled linearly and used to correct sample spectra. The magnitude of the observed drift for the
299 X26A monochromator was of similar magnitude to that reported by Cottrell et al. (2009). Sample
300 spectra were not acquired in the first hour following electron injection of the storage ring, when

301 monochromator thermal drift is most non-linear. Resultant XANES spectra covering the entire
302 energy range studied are shown in Figure 1.

303 **Datasets**

304 Two distinct processing treatments were performed to determine the sensitivity of the
305 predictions of $\text{Fe}^{3+}/\Sigma\text{Fe}$ to pre-processing routines, specifically edge-step normalization and
306 over-absorption correction. **Minimal Treatment** required the least user input and included
307 normalization to incident beam intensity, edge-step normalization to an average of the last five
308 data points in the spectrum, and no over-absorption correction. **Full Treatment** included
309 normalization to incident beam intensity, edge-step normalization with a polynomial fit to a user-
310 specified portion of the post-edge, and correction for over-absorption using the PAXAS software
311 described below.

312 Each treatment was performed eight ways, and its effect on the prediction of $\% \text{Fe}^{3+}$ was
313 evaluated:

- 314 1. Predict each X orientation spectrum from all other X orientation spectra.
- 315 2. Predict each Y orientation spectrum from all other Y orientation spectra.
- 316 3. Predict each Z orientation spectrum from all other Z orientation spectra.
- 317 4. Predict each X or Y oriented spectrum from all other X or Y oriented spectra.
- 318 5. Predict each X, Y, or Z-oriented spectrum from all other X, Y, and Z-oriented
319 spectra.
- 320 6. Predict each spectrum from crystals that were randomly-oriented using all other data
321 for which crystals were randomly-oriented.
- 322 7. Predict each spectrum of samples for which crystals were randomly-oriented from
323 spectra of all X, Y, and Z-oriented spectra.

324 8. Predict each oriented or randomly-oriented crystal spectrum from all other spectra of
325 oriented and randomly-oriented samples.

326 Prediction of $\text{Fe}^{3+}/\Sigma\text{Fe}$ was undertaken for four univariate and three multivariate models
327 for each of the two pre-processing treatments and eight subsets of spectra, as described below.

328 **Data Pre-Processing**

329 The two different methods of edge-step normalization used in the Minimal Treatment
330 (average of the last five data points) and Full Treatment (the more widely used polynomial fit)
331 were compared in case significant oscillations continued beyond 7220 eV where the scans ended.
332 If significant oscillations remained past 7220 eV, error could result in polynomial modeling of
333 the post-edge due to uncertainty in the location of appropriate nodes required to constrain the
334 polynomial function. Normalizing to the last five data points as in the Minimal Treatment
335 eliminates the need for the user to specify node locations, though could result in poor modeling
336 of the background shape for spectra with slope in the post-edge.

337 Examination of the raw spectra (normalized to incident beam intensity only) shows that
338 these amphibole spectra are similar in the shape of the post-edge regardless of oxidation state
339 and have a relatively flat slope (Figure 1, top). This suggests that a simple scaling of intensity as
340 in the Minimal Treatment rather than a correction for shape will suffice to normalize spectra.
341 Indeed, simply normalizing these raw spectra to total spectral intensity (dividing each pixel by
342 the sum of all pixels in the spectrum), brings all spectra within 20% in magnitude at 7140 eV, the
343 region of greatest spread (Figure 1, bottom). This indicates that scaling for variations in signal
344 return due to beam-to-sample coupling and inter-session variability accounts for the majority of
345 signal variation. The Full Treatment spectra in Figure 2 do have intensity variation at 7220 eV,
346 suggesting that some oscillation continued beyond 7220 eV. Predictions of $\text{Fe}^{3+}/\Sigma\text{Fe}$ for Full

347 Treatment and Minimal Treatment models are comparable, however, suggesting that differences
348 in edge-step normalization methods have little impact for this data set.

349 Spectra used for prediction of $\text{Fe}^{3+}/\Sigma\text{Fe}$ by Full Treatment Models (see description above)
350 were processed using the PAXAS (Python Analysis for XAS) software package written for this
351 project by Mirna Lerotic. The program automates, as a batch process, I_0 and edge-step
352 normalization for XANES spectra, correction for over-absorption effects using the FLUO
353 algorithm (Haskel 1999), and spectral fitting including background removal and Gaussian fitting
354 of pre-edge centroids, fitting of the rising edge and the white line of the absorption spectra.
355 PAXAS works in batch processing mode taking as input an ascii list of files that points to the file
356 name of raw spectra data (multi-column data of energy bins, fluorescence intensities and incident
357 flux intensities), a listing of sample compositions for OA corrections and optional energy shifts
358 for each spectra. Input data files are in the form of $\chi\mu$ (*.xmu) format as output by the ATHENA
359 program as “project files.” Output is as normalized $\mu(E)$ (Ravel and Newville 2005), though
360 PAXAS can also fit peaks to the pre-edge region. PAXAS assumes that input data has already
361 been corrected for detector dead-time effects. The software is currently being configured to
362 output predicted % Fe^{3+} using the optimal algorithm described in this paper for amphiboles.

363 Background removal and edge-step normalization in PAXAS were performed using a
364 linear fit to the pre-edge region (~7045-7095 eV) and a third-order polynomial fit to the post-
365 edge region (~7190-7210 eV) (using the algorithm of Ravel and Newville 2005). The edge-step
366 normalization constant, $\mu_0(E_0)$, represents the value of the background function evaluated at the
367 absorption edge energy E_0 . It is determined by extrapolating the pre- and post-edge fits to E_0 and
368 subtracting the E_0 -crossing of the pre-edge fit from the E_0 -crossing of the post-edge fit. The pre-

369 edge fit is extrapolated to all energies and subtracted from $\mu(E)$. These pre-edge subtracted data
370 are divided by $\mu_0(E_0)$ to yield background removed, edge-step normalized spectra.

371 Spectra were corrected for over-absorption (OA) using an adaptation of the FLUO
372 algorithm (<http://www.aps.anl.gov/~haskel/fluo.html>) as implemented in PAXAS. Over-
373 absorption is the reason why transmission x-ray absorption analysis is typically the preferred
374 XAS technique at high absorber concentrations. Over-absorption is sometimes referred to as
375 “self-absorption” but that term is something of a misnomer because the observed attenuation has
376 nothing to do with re-absorption of the fluorescence radiation (Manceau et al. 2002). In fact, the
377 absorption of the fluorescence is independent of the incident energy, and hence does not
378 contribute to any non-linearity. What is important is that the penetration depth for the incident
379 radiation depends on the quantity to be measured, which changes over the energy range of the
380 absorption edge. The effect of over-absorption in high-Fe (i.e., most geologically-relevant)
381 samples is to reduce the ratio of feature height to background relative to that predicted from a
382 simple correlation between X-ray intensity and composition. As part of this study, we seek to
383 test the importance of this correction on quantitative results for predicting Fe^{3+} contents.
384 Accordingly, the major element compositions used in the correction are shown in Table 2.
385 Absorption cross-sections used to approximate the absorption coefficient for OA correction are
386 from McMaster et al. (1969). PAXAS assumes no OA correction is required when no
387 composition is supplied. Background removal, edge-step normalizations and OA corrections
388 were all conducted in a manner so as to provide comparable normalizations and corrections to
389 those used for data presented for garnets in Dyar et al. (2012).

390 **Univariate models (simple linear regression)**

391 Four simple linear regression models (SLR) were employed to predict $\text{Fe}^{3+}/\Sigma\text{Fe}$ from
392 minimally and fully pre-processed spectra using the eight data subsets described above: 1) area-
393 normalized pre-edge centroid method, 2) absorption edge energy method, 3) intensity ratio
394 method, and 4) slope method. For all SLR models, a calibration curve was generated between the
395 selected predictor variable and $\text{Fe}^{3+}/\Sigma\text{Fe}$. All spectra belonging to the sample being predicted
396 were left out of the calibration curve when predicting that sample.

397 For the area-normalized pre-edge centroid method, the pre-edge region defined in the
398 PAXAS configuration file is extracted. The background (the contribution of the main edge to the
399 pre-edge spectrum) is fitted with a linear offset and a portion of a Lorentzian line (Hecht 1987)
400 and subtracted, with no constraints on wavelength. Pre-edge peaks are fitted using a user-defined
401 number of Gaussian curves (2 or 3 in this study, depending on the spectrum). An area-
402 normalized centroid energy is calculated for each spectrum as the sum of the products of each
403 Gaussian relative area (expressed as a percentage) and its centroid energy, as done by Wilke et
404 al. (2001):

$$405 \quad \text{Centroid}_{\text{area-normalized}} = \% \text{Area}_{\text{peak1}} \times \text{Centroid}_{\text{peak1}} + \% \text{Area}_{\text{peak2}} \times \text{Centroid}_{\text{peak2}} + \% \text{Area}_{\text{peak3}} \times \text{Centroid}_{\text{peak3}}.$$

406 The area-normalized centroid energies were then used as input for simple regression expressions
407 to quantify $\% \text{Fe}^{3+}$.

408 **Multivariate models**

409 Two different multivariate techniques were used to process the XANES data. The first is
410 partial least squares (PLS), also known as projection to latent structures, which was developed
411 for use in situations where explanatory variables (p) significantly outnumber observations (N). It
412 has been used to analyze data from a variety of types of spectroscopy, including, but not limited
413 to, laser-induced breakdown spectroscopy (Clegg et al 2009, Dyar et al. 2012), near infrared
414 reflectance (NIR) spectroscopy (Kramchote et al. 2014, Zhang et al. 2015), Fourier transform

415 infrared (FTIR) spectroscopy (Hayes et al. 2014, Anjos et al. 2015), and Fourier transform-
416 Raman (FT-Raman) spectroscopy (Lopez-Reyes et al. 2014). PLS calculates components that
417 maximize the covariance between the feature and response matrices (Wegelin 2000). It is
418 especially well suited for problems with many highly correlated features and multiple responses
419 (Erdas et al. 2010, Kalivas 1999).

420 PLS sequentially chooses directions, or components, of maximal covariance from the
421 feature matrix, \mathbf{X} , and the response matrix, \mathbf{Y} , to determine the model coefficients using a two-
422 step process. The first step is the shrinkage step, in which the shrinkage penalty determines the
423 number of factors to be included in the regression. This shrinks the feature matrix by projecting
424 it from the original p -dimensional space into a smaller q -dimensional vector space. In the context
425 of this project, $p = 434$, the number of channels (wavelength values) at which the signal is
426 measured, and q , the number of components, is either allowed to vary from 1-10 or held constant
427 at some generalized value within that range. The choice of an appropriate number of components
428 does not relate directly to any of the variables (such as %Fe³⁺) but rather is analogous to the
429 order of a polynomial line used to fit a complex set of data. As in that example, higher numbers
430 of components train the model more closely to the specific training set, while use of fewer
431 components makes the model more generalizable. The components themselves are a set of linear
432 combinations of channel intensities that best explain the variation in the data set. They are
433 constructed by the algorithm, which solves for the best linear combination of channels. The
434 second step follows ordinary least squares by regressing the response on the components
435 generated in the first step to minimize the residual sum of squared error. For this project, a single
436 response model, PLS-1, was trained for prediction of our variable of interest, which is Fe³⁺/ΣFe.

437 **Lasso.** Least absolute shrinkage and selection operator (lasso) regression is an ordinary
438 least squares regression model with an l_1 penalty on the model coefficients to induce sparsity
439 (Hastie et al 2009). The lasso provides a sparse model by shrinking some coefficients and setting
440 most other coefficients to zero. In other words, the lasso removes channels (in our application,
441 energies) where the signal is not useful for predicting %Fe³⁺. It is assumed that a smaller (<434)
442 subset of the predictor variables is driving the prediction results. Thus, other coefficients can be
443 excluded from the model (i.e., set to zero) with no significant performance loss. This reduces a
444 sizable, largely uninterpretable model to a sparse, more interpretable model:

445 To calculate its model coefficients, the lasso fits a linear model

$$446 \hat{y} = b_0 + (b_1 \times x_1) + (b_3 \times x_3) + \dots (b_p \times x_p) \quad (1)$$

447 with a goal of minimizing $\sum(y - \hat{y})^2$ and keeping the sum of the absolute values of the weights
448 at a minimum, such that $\sum|b_j| \leq s$. Adding that constraint on s as a boundary condition to
449 ordinary least squares prevents the model from overfitting the training data.

450 Choice of a value for s is difficult, so an alternate parametrization is helpful. The lasso penalty,
451 L_q , is used to select specific channels (wavelengths) for each element that explain the most
452 variance in its predicted concentration. The lasso penalty, L_q , can be generalized as:

$$453 b^* = \operatorname{argmin}_b \left\{ \sum_{i=1}^n (y_i - b_0 - \sum_{j=1}^p x_{ij} b_j)^2 + \lambda \sum_{j=1}^p |b_j|^q \right\} \text{ for } q \geq 0. \quad (4)$$

454 Here b^* is the value that minimizes the overall error in y and the weights of the individual
455 channels, x_{ij} is the i th example in the j th channel, λ (sometimes called α) is a variable term that
456 restrict the sparsity of the result, and q is set to one, which shrinks some coefficients and sets
457 other, less influential coefficients to zero. For problems with many features, the lasso can
458 eliminate noisy features that may otherwise hinder the model. These parsimonious models have

459 shown to be effective in many types of chemometric models (Andries 2013, Filmozer et al.
460 2012).

461 The open-source machine learning Python library Scikit-learn (Pedregosa et al. 2011)
462 was used to train and test all models.

463 RESULTS

464 Spectra from oriented and randomly-oriented amphiboles were acquired and processed
465 using the Full Treatment and Minimum Treatment methods described above (Tables 3, 4, and 5).
466 The only exception was that only Full Treatment pre-edge data were fit for determination of the
467 area-normalized pre-edge centroid for comparison with published calibrations processed in the
468 same manner. Several different strategies for predicting $\text{Fe}^{3+}/\Sigma\text{Fe}$ were undertaken.

469 Area-Normalized Pre-edge Centroid Energy vs. $\text{Fe}^{3+}/\Sigma\text{Fe}$

470 In this method, component peaks are fit to the pre-edge, and then an area-normalized
471 centroid energy is calculated for use in calibration. This energy is the point dividing the total
472 integrated intensity in half (Table 3). This is the method first used by Bajt et al. (1994) and
473 adapted and described in detail by many subsequent users including Wilke et al. (2001) and
474 Cottrell et al. (2009). The highest R^2 value for a fit of area-normalized pre-edge centroid fit to
475 predicted $\% \text{Fe}^{3+}$ vs. true $\% \text{Fe}^{3+}$ was 0.91 for predictions of Fe^{3+} in Y-oriented crystals from other
476 Y-oriented crystals (Figure 3A, B). The root of the mean-squared errors (RMSE) of the eight
477 different sample combinations ranged from 9.7-18.1% (absolute, in units of $\% \text{Fe}^{3+}$). So even
478 when like orientations are used to predict the same optical orientations, use of a single peak
479 centroid based on its area-normalized energy does not produce very accurate results.

480 The reason for this high error is apparent in Figure 4, which shows the variations in pre-
481 edge intensity and position as a function of orientation for seven representative samples. The
482 three heat treated, ["HT"] samples are all nearly completely oxidized, yet their peak intensities

483 are only somewhat similar to one another. The shape of the pre-edge is dramatically different for
484 each sample at each orientation.

485 **Alternate Methods for Predicting Fe³⁺ using Linear Correlations**

486 Berry et al. (2010) evaluated two other univariate methods for predicting Fe³⁺ using XAS
487 spectra. Note that those studies used only garnets, which are isotropic. Results of similar
488 methods applied to our amphiboles are shown in Figure 5 and accuracies and R² values are given
489 in Table 4.

490 The absorption edge energy method is based on work done with garnet spectra by Berry
491 et al. (2010). They found high R² correlation between Fe³⁺/ΣFe and the energy at which the
492 absorption edge reaches a normalized intensity of 0.9 for each spectrum, with samples with
493 greater Fe³⁺/ΣFe reaching that intensity at higher energies. In this study, R² with Fe³⁺/ΣFe was
494 calculated for all absorption edge energies at normalized intensities from 0.04 – 1.4 at an interval
495 of 0.01. The absorption edge energy with the highest R² was used to predict Fe³⁺/ΣFe. The best-
496 performing absorption edge model is for full treatment pre-processing, predicting Z-oriented
497 spectra from Z-oriented spectra. RMSE for this model is 3.7% Fe³⁺ and R² between true and
498 predicted Fe³⁺/ΣFe is 0.99 (Table 4). Energy at a normalized intensity of 0.29, corresponding to a
499 range of 7119.2 – 7122.4 eV for the Z-oriented spectra, was selected as the best predictor of
500 Fe³⁺/ΣFe.

501 For the intensity ratio method, normalized intensity at each channel was divided by
502 normalized intensity at every other channel. R² was calculated between those 41,209 ratios per
503 spectrum and Fe³⁺/ΣFe, and the ratio with the highest correlation was used to predict Fe³⁺/ΣFe.
504 This method was also inspired by Berry et al. (2010), who found high correlation between
505 normalized intensity ratio at two spectral features that occur at 7138.4 and 7161.7 eV in garnet

506 spectra. While acknowledging that this is a somewhat ad-hoc approach because the features lie in
507 the region caused by multiple scattering processes, Berry et al. (2010) plotted the ratio of
508 intensities at those two wavelengths vs. Fe^{3+} , which resulted in a useful prediction of Fe^{3+} . Our
509 method examines every possible intensity ratio for correlation with $\text{Fe}^{3+}/\Sigma\text{Fe}$ regardless of the
510 presence or absence of distinguishing spectral features. The best-performing intensity ratio
511 model is also for full treatment pre-processing, predicting Z-oriented spectra from Z-oriented
512 spectra. RMSE for this model is 1.7% Fe^{3+} and R^2 between true and predicted $\text{Fe}^{3+}/\Sigma\text{Fe}$ is 1.00
513 (Table 4). The ratio of normalized intensity at 7119.5 eV (main edge) to that at 7149.0 eV (post-
514 edge) was selected as the best predictor of $\text{Fe}^{3+}/\Sigma\text{Fe}$ for the Z-oriented spectra.

515 For the slope method, the first derivative of the spectrum was computed for every
516 channel. The slope at the channel with the highest R^2 was used to predict $\text{Fe}^{3+}/\Sigma\text{Fe}$. This method
517 was undertaken because samples with greater $\text{Fe}^{3+}/\Sigma\text{Fe}$ appear to have sharper features in both
518 the pre-edge and the main edge. The best-performing slope model is also for full treatment pre-
519 processing, predicting Z-oriented spectra from Z-oriented spectra. RMSE for this model is 6.0%
520 Fe^{3+} and R^2 between true and predicted $\text{Fe}^{3+}/\Sigma\text{Fe}$ is 0.97 (Table 4). The slope at 7117.2 eV
521 (between pre-edge and main edge) was selected as the best predictor of $\text{Fe}^{3+}/\Sigma\text{Fe}$ for the Z-
522 oriented spectra.

523 **Partial Least Squares**

524 While working with the existing methods for Fe^{3+} predictions discussed above, it became
525 apparent that more sophisticated statistical analysis of these data might improve our results, as
526 was the case for garnet spectra detailed in Dyar et al. (2012). PLS models were built for each
527 data set (Table 5) in two different ways. The first (labelled “PLS” in Table 5) tuned the
528 hyperparameter, q , differently for each model using the number of components among the first

529 ten that provides the global minimum RMSE. The second set of models (“PLS*” in Table 5)
530 used a constant number of components (6, chosen from the most common value of the global
531 minimum) in all models. PLS coefficients for each channel are superimposed on plots of all
532 spectra in each model in Figure 6. The largest positive and negative coefficients in each PLS
533 model lie at predictor channels in the main edge and EXAFS region rather than in the pre-edge.

534 **Lasso**

535 Lasso models were also built for both minimal and full treatments of all data, in eight
536 combinations as listed in Table 5 and shown in Figure 7. Relative performance of the lasso
537 models is in many cases inferior to that of the PLS models. However, the lasso models are
538 extremely sparse and thus likely to be more generalizable. For example, the model of spectra
539 with the beam polarization along the Y optical orientation uses only five channels, suggesting
540 that all the information needed to predict Fe^{3+} with Y-oriented samples is contained in only five
541 channels – likely representing important transitions in that orientation. Moreover, Figure 8 shows
542 that the eight different models are all picking nearly the same channels, with only small offsets
543 between the full and minimal treatment models that result from the over-absorption correction.
544 Theory has not yet advanced to the point of understanding the transitions to which these energies
545 correspond in such a complex mineral structure with four different sites for Fe. However, it is
546 clear that the XAS energies at channels corresponding to 7120, 7153, and 7217 eV for the
547 minimal models and 7129, 7154, 7162, and 7194 eV for the full treatment models must be
548 associated with the phenomena (key transitions) that differentiate between Fe^{2+} and Fe^{3+} in
549 amphiboles.. Reducing the number of channels needed for Fe^{3+} prediction to such a small
550 number is critically important because it enables rapid analyses and facilitates development of
551 methodology for acquisition of high-resolution redox maps with 1- μm pixel sizes.

552 **First Derivative Models for PLS and Lasso**

553 The multivariate models clearly depend upon data channels in the main edge and EXAFS
554 regions to predict Fe^{3+} contents. To test whether this occurs because of the absolute magnitude of
555 the peaks, we ran the full set of PLS and Lasso models on first derivatives of the spectra rather
556 than raw spectral intensity to see if the channels that are picked are the same. Results are shown
557 in Figure 9 and Table 5. They demonstrate that multivariate models based on first derivative
558 spectra do not choose channels in the pre-edge region either, and moreover, they produce results
559 that are comparable to but slightly less accurate as measured by RMSE.

560 **DISCUSSION**

561 Amphiboles are either monoclinic (like those studied here) or orthorhombic minerals,
562 with varying atom densities at different orientations that gives rise to the familiar pleochroism
563 observed in amphiboles in thin section. These variations are manifested in optical spectra of
564 amphiboles, which exhibit strong variations as a function of orientation because specific
565 electronic interactions are most favored along specific directions in the crystal structure. A strong
566 absorption band at $\sim 1,000$ nm corresponds to Fe^{2+} in the $M(4)$ site and is most active in the β
567 ($=Y$) optical orientation across the I-beams in the amphibole structure. Optical wavelength
568 interactions from the Fe^{2+} $M(1)$ - $M(3)$ site band are strongest in the sharp peak at 1,400 nm,
569 which arises from Fe interactions along the $\alpha \sin \beta$ (closest to X) orientation perpendicular to the
570 plane of the I-beams (Figure 10). XANES spectra should also reveal atomic interactions with
571 electromagnetic radiation of much higher energy. This is suggested in our spectra, in which the
572 highest energy pre-edge peak (ca. 7114.1 eV) is consistently the most intense in the X
573 orientation, consistent with it being caused by Fe^{2+} hosted at the $M(1)$ - $M(3)$ sites. However,

574 sample Z2124 HT, which contains 100% Fe³⁺, also has a feature at this energy, so there must
575 also be some contribution there from Fe³⁺.

576 Within the chemistry literature, Fe XANES pre-edge spectra have been modeled based on
577 molecular orbital calculations; for simple compounds, normalized pre-edge positions and
578 intensities can successfully be predicted. For example, Randall et al. (1995) quantified the
579 coordination number and symmetry of Fe²⁺ atoms in synthetic high-spin Fe²⁺ complexes, and
580 Westre et al. (1997) used ligand field theory to describe systematic relationships between spin
581 state, oxidation state, and site geometry and the energy (i.e., position), splitting, and intensity
582 distribution in a large variety of ferrous and ferric model compounds. These workers and many
583 others subsequently have shown that the Fe K edge is extremely sensitive to the electronic
584 structure of the Fe cation. In general, pre-edge intensities are greater in Fe³⁺-bearing minerals
585 because of the additional hole that is present in their ground state. This is also consistent with the
586 observation that the highest energy peak in our pre-edge fits should be assigned to Fe³⁺ as noted
587 in the previous paragraph.

588 Moreover, Westre et al. (1997) show that distortions from ideal octahedral symmetries to
589 tetrahedral and square pyramidal geometries (as are found in most mineral spectra) allow for $3d$
590 $\rightarrow 4p$ mixing, and affect both the intensity and energy distribution in the pre-edge region. The
591 effect of symmetry on pre-edge intensity is commonly observed in minerals. For example, Fe²⁺
592 with a perfect octahedral coordination would have no pre-edge; we have observed this scenario
593 in wüstite XAS data (unpublished data). If site geometry is the dominant effect on pre-edge
594 intensity and specific pre-edge features result from the distinct M sites in amphiboles, then the
595 distortion in cation polyhedra ought to correlate with the intensity of peaks in the pre-edge.

596 Because we have done SREF of seven of the samples used in this study, we are able to address
597 this issue, albeit inconclusively.

598 The geometry of coordination polyhedra can be described using two parameters devised
599 by Robinson et al. (1971), who quantified polyhedral distortion using data derived from single
600 crystal structure refinement. The first parameters is angular variance, σ , calculated using the
601 expression, where

$$602 \quad \sigma = \frac{\sum_{i=1}^n (\theta_i - \theta_{avg.})^2}{n-1}. \quad (2)$$

603 Here θ_i is the measured O-cation-O angle in the crystal structure (there are $n = 12$ angles in a 6-
604 coordinated site), and θ_{avg} is theoretical value for a perfect octahedron (all angles are 90°). Units
605 are in degrees squared. Values of σ directly reflect how distorted the polyhedra are. The second
606 parameter is the quadratic elongation (λ), where

$$607 \quad \lambda = \sum_{i=1}^n \left(\frac{l_i}{l_0} \right)^2 / n. \quad (3)$$

608 In this expression, l_i is the measured cation- oxygen bond distance (where $n = 6$ for 6-
609 coordination) and l_0 is the bond distance in a perfect (undistorted, equal volume) octahedron.
610 Values for octahedral λ range from ~ 1.00 for wustite and garnets, up to 1.06 for some olivines
611 and pyroxenes, and can be as high as 1.15 in staurolite, which indeed has a very intense pre-edge
612 (Wilke et al. 2001). This parameter is unitless. Of the two parameters, quadratic elongation is
613 generally considered to provide the best measure of polyhedral distortion (Robinson et al. 1971).
614 Note also that octahedra containing smaller trivalent and divalent cations (e.g., Al^{3+} , Fe^{3+} , and
615 Mg^{2+}) are generally less distorted than those containing larger divalent cations (Robinson et al.
616 1971; Brown 1970). If polyhedral distortion is the dominant factor controlling peak intensity,
617 then large values of λ and σ ought to relate to intense peaks.

618 Table 6 shows occupancies of Fe cations in the $M(1)$ - $M(4)$ sites of seven of the samples
619 studied here, and Figure 11 plots summed pre-edge areas against λ and σ for the [6-coordinated]
620 $M(1)$, $M(2)$, and $M(3)$ polyhedra. Overall, there is little correlation between λ and the pre-edge
621 area. For the $M(3)$ octahedron, there is a clear inverse correlation between λ ($R^2 = 0.90$) and
622 σ ($R^2 = 0.91$) versus peak area. Perhaps this relationship occurs because the $M(3)$ polyhedron - in
623 the center of the strip (Figure 12) – when occupied by Fe^{3+} , is strongly affected by the
624 dimension/conformation of the other octahedra, in particular of $M(1)$, where most of the
625 oxidation related to deprotonation occurs. Overall, these data suggest that the dominant control
626 on peak area is not site distortion. However, note that in every pair of natural vs. heat-treated
627 spectra, at every orientation, the maximum peak intensity does correlates with the amount of Fe^{3+}
628 present (Figure 4). Thus, valence state is a far more important factor in pre-edge intensity than
629 symmetry, at least for the amphibole group studied here.

630 IMPLICATIONS

631 **Recommendations for Measuring Fe^{3+} in Amphiboles using XAS**

632 Figure 13 shows a comparison of the accuracy of all models used in this study for
633 predicting Fe^{3+} contents in amphiboles. The most important conclusion of this research is that it
634 provides clear evidence for the utility of the entire XANES region in predicting Fe valence
635 states. Our PLS and lasso loading and coefficients show that there is key diagnostic information
636 in other regions of their spectra arising from changes to the local structural environment resulting
637 from the difference in size and charge between Fe^{2+} and Fe^{3+} . The community would benefit
638 greatly from a new study of powdered mineral spectra of reference materials using multivariate
639 analyses to predict valence state and, potentially, coordination number. These authors will
640 support that effort in any way possible.

641 In the meantime, the model from this study will be made broadly available for studies
642 associated with interpreting conditions of geological formations of amphiboles; the PAXAS code
643 and associated multivariate models are available upon request from the senior author. Another
644 important use of this technique will be to health-related fields for the study of asbestiform
645 minerals, many of which are amphibole species (Gunter et al. 2007). Gunter et al. (2011) used
646 synchrotron methods to document differences in the oxidation state of Fe between asbestiform
647 and non-asbestiform samples, and suggested that iron oxidation, mineral morphology, and
648 potential health effects may all be interrelated. Implementation of our method for measuring
649 redox states in amphibole particles will enable further research to understand the role of
650 oxidation state in the causation of disease between these differing morphologies.

651 Results of this study also have broad implications for many types of synchrotron
652 applications in which single phases are studied without careful attention to orientation effects. As
653 with optical spectra of the visible region and infrared spectra, pleochroism effects as evidenced
654 in XAS transitions are significant and ubiquitous in anisotropic materials. Many workers have
655 attempted to document orientation effects by rotating their samples on the stage, but this practice
656 can be misleading. At best, when the stage is oriented at a 90° angle to the beam, rotation
657 samples two of the three optical orientations of a crystal, but only if it is orthorhombic. Most
658 microprobe beamlines are configured with the beam impinging on the sample at a 45° angle with
659 fluorescence detectors placed at 90° to the incident beam and in the plane of the storage ring to
660 reduce measured X-ray scatter and significantly improving measured peak to background for a
661 given emission line. In this geometry, rotation within the sample plane simply samples assorted
662 angles within the crystal. To acquire spectra from at least two optical orientations, a back-
663 fluorescence configuration in which the beam impinges on the thin section's surface at a 90°

664 angle with the beam co-located with the stage's rotation axis is optimal. This geometry is
665 analogous to that used in the current study as depicted in Figure 1 of Dyar et al. (2002b) and used
666 in several experimental papers by Cibin et al. (2006, 2010).

667 Many of the previous calibrations for predicting Fe^{3+} on the basis of pre-edge
668 spectroscopy are limited to analyses of powders (e.g., Galois et al. 2001, Wilke et al. 2001), but
669 this limits their usefulness in petrologic contexts where it is desirable to analyze minerals in situ
670 in thin sections. Dyar et al. (2002a) determined that the effect of orientation on calculated
671 $\text{Fe}^{3+}/\Sigma\text{Fe}$ would be $\pm 10\text{-}20\%$ errors in randomly-oriented crystals using the position of the peak
672 area-normalized pre-edge. In this study, Table 4 quantifies this effect for seven different
673 prediction methods. Results show that the worst errors ($\pm 33\%$ and $\pm 11\%$ Fe^{3+} relative to total Fe)
674 arise from predicting Fe^{3+} in randomly-oriented crystals using a calibration based only on spectra
675 acquired with the beam polarized along X, Y, and Z using the minimal and full treatment
676 models, respectively. The situation improves when the entire data set (spectra of oriented and
677 randomly-oriented crystals) is used for training, with RMSEP errors of $\pm 14\%$ and $\pm 7\%$ Fe^{3+} ,
678 again respectively. These error bars do not come close to the $\pm 1\text{-}3\%$ absolute errors associated
679 with $\% \text{Fe}^{3+}$ measurements from Mössbauer spectroscopy and wet chemistry. Although the $\pm 7\%$
680 error using the full treatment model is probably the best that can be achieved for random grains
681 in a thin section using currently-available data and technology, it will still be useful for many
682 applications, and is markedly better than picking out grains and powdering them for analysis by
683 other methods! Combination of XANES results with in-situ EBSD measurements or single-
684 crystal X-ray diffraction would have the potential to provide precise orientation data for all spots
685 measured in thin section.

686 **Comparison with Garnet Results**

687 Given the success of the lasso predictions for the amphiboles when orientation was held
688 constant, we undertook lasso predictions of the garnet data set from Dyar et al. (2012) for
689 comparison. The 19 samples studied cover a range from almandine, andradite, grossular, and
690 melanite. Results are shown in Figures 14 and 15. Two themes are again apparent. Prediction of
691 Fe^{3+} utilizes primarily the main edge regions of the spectra rather than the pre-edge, as indicated
692 by the positions of the vertical red lines in Figure 15. Note that the number of channels needed to
693 accurately predict Fe^{3+} is larger for garnet than for amphiboles. This difference may be explained
694 by the wide range of garnet compositions represented in the study, or by a large number of
695 possible transition for garnet relative to amphibole – theory is insufficient to explain. Second, for
696 garnets the lasso provides significantly more accurate measurement of $\text{Fe}^{3+}/\Sigma\text{Fe}$ than PLS, with
697 an error of $\pm 0.01\%$ Fe^{3+} . This success of this model can be attributed to both the isometric nature
698 of the garnet structure and the fact that only two sites are present. However, Dyar et al. (2016)
699 showed that Fe^{3+} contents in silicate glasses with widely-ranging compositions and Fe^{3+} from 0-
700 100% could be predicted with an accuracy of $\pm 3.6\%$ Fe^{3+} (absolute) even though glass by
701 definition has a wide variety of sites for Fe^{2+} and Fe^{3+} . These results reinforce the conclusions of
702 the amphibole work, which also show that when orientation effects are mitigated (i.e., for
703 predicting Y from Y), extremely accurate results can be obtained.

704 The success of this paper and the previous work on garnet suggests that multivariate
705 analysis may be the key to quantifying Fe redox states across a wide variety of geological (and
706 other) materials. The contrast between the garnet, putative glass, and amphibole results
707 highlights the fact that anisotropy is the primary source of error in predicting Fe^{3+} in amphiboles.
708 Optimal accuracy in thin section analyses can be obtained by carefully orienting crystals of
709 unknowns with respect to their optical orientations and then interpreting those results using a

710 model built on standards also acquired at the same orientation. If random orientations are probed
711 without knowledge of their orientations, then reduced accuracy must be accepted.

712 This study also highlights the need for further analogous studies of other mineral groups
713 commonly studied at microscales. The magnitude of error introduced by failure to correct for
714 crystal orientation will likely scale with the magnitude of optical birefringence (the difference in
715 refractive index between two directions of a crystal), which is a convenient measure of
716 dissimilarity between two orientations. For example, minerals in the feldspar group are
717 framework silicates in which all the corners of every Si and Al tetrahedron are shared. This
718 creates a 3-D tetrahedral network, with similar electron densities and charges in all directions. As
719 a result, feldspars have very low birefringence. So in feldspars, there should not be such dramatic
720 differences in XAS spectra acquired along X, Y, and Z orientations. At the other extreme (e.g.,
721 Dyar et al. 2002), layer silicates have only three of the four corners of the tetrahedra shared. In
722 minerals like biotite and muscovite, there are roughly similar atomic and electronic densities
723 within the sheets (i.e., the *a-b* plane), so a mica section where the light vibrates only in the sheet
724 will have low birefringence and a small difference between the two crystal orientations.
725 However, a grain oriented where one of the orientations represents light vibrating perpendicular
726 to the sheets in the *a-b* plane (i.e., along *c*), shows marked birefringence. This would be
727 manifested in XAS by similar spectra in the X and Y directions that would be quite different
728 from those acquired with the vibration direction along Z. Finally, chain silicates like pyroxene,
729 which share only two of four corners of their tetrahedral, usually have the largest refractive index
730 and highest retardation along the chains. So maximum retardation will occur when looking at
731 any slice that includes the direction along which the chains lie, but X, Y, and Z would all be
732 expected to be different. So for biopyribole groups like layer silicates and pyroxenes, it is

733 imperative that XAS data from end-member optical orientations be acquired to ensure optimal
734 accuracy in predicting Fe^{3+} .

735 Although detailed studies like this current paper are time-consuming and difficult, they
736 are necessary to obtain accurate and truly quantitative analyses of $\text{Fe}^{3+}/\text{Fe}^{2+}$ at microscales. The
737 potential pay-off for these detailed studies will be the unveiling of a new capability for
738 understanding variations of Fe redox state and oxygen fugacity at micron and sub-micron scales.

739 **ACKNOWLEDGMENTS**

740 We are grateful to Katy Evans and an anonymous reviewer for their thoughtful comments
741 on this manuscript, which greatly improved it. We thank Paul Moore for the use of samples
742 PBM-1B, -2, -4, and -6, and George Rossman for permission to show his visible-region
743 amphibole spectra. We are grateful for support of this research from NSF grants EAR-0809459
744 and EAR-1219761. Portions of this work were performed at Beamline X26A, National
745 Synchrotron Light Source (NSLS), Brookhaven National Laboratory. X26A is supported by the
746 Department of Energy (DOE) - Geosciences (DE-FG02-92ER14244 to The University of
747 Chicago - CARS). Use of the NSLS was supported by DOE under Contract No. DE-AC02-
748 98CH10886. Finally, graduate student support for this project came from NASA grant
749 NNA14AB04A, the RIS4E Virtual Institute, publication #xxxx.

750 **REFERENCES**

751 Andries, E. (2013) Sparse models by iteratively reweighted feature scaling: a framework for
752 wavelength and sample selection. *Journal of Chemometrics*, 27, 50-62.

753 Anjos, O., Campos, MG., Ruiz, P.C., and Antunes, P. (2015) Application of FTIR-ATR
754 spectroscopy to the quantification of sugar in honey. *Food Chemistry*, 169, 218-223.

- 755 Bajt, S., Sutton, S.R., and Delaney, J.S. (1994) Microanalysis of iron oxidation states in silicates
756 and oxides using X-ray absorption near edge structure (XANES). *Geochimica et*
757 *Cosmochimica Acta*, 58, 5209-5214.
- 758 Beck, P., De Andrade, V., Orthous-Daunay, F.-R., Veronesi, G., Cotte, M., Quirico, E., and
759 Schmitt, B. (2012) The redox state of iron in the matrix of CI, CM, and metamorphosed
760 CM chondrites by XANES spectroscopy. *Geochimica et Cosmochimica Acta*, 99, 305-
761 316.
- 762 Berry, A.J., Yaxley, G.M., Woodland, A.B., and Foran, G.J. (2010) A XANES calibration for
763 determining the oxidation state of iron in mantle garnet. *Chemical Geology*, 278, 31-37.
- 764 Bigeleisen, J., Perlman, M.L., and Prosser, H.C. (1952) Conversion of hydrogenic materials to
765 hydrogen for isotopic analysis. *Analytical Chemistry*, 24, 1356-1357.
- 766 Bonadiman, C., Nazzareni, S., Coltorti, M., Comodi, P., Giuli, G., and Faccini, B. (2014) Crystal
767 chemistry of amphiboles: Implications for oxygen fugacity and water activity in
768 lithospheric mantle beneath Victoria Land, Antarctica. *Contributions to Mineralogy and*
769 *Petrology*, 167, 984.
- 770 Booth, C.H., and Bridges, F. (2005) Improved self-absorption correction for fluorescence
771 measurements of extended X-ray absorption fine-structure. *Physica Scripta*, T115, 202-
772 204.
- 773 Brouder, C.J. (1990) Angular dependence of X-ray absorption spectra. *Journal de Physique*, 2,
774 701-738.
- 775 Brown, G.E. Jr. (1970) The crystal chemistry of the olivines. Virginia Polytechnic Institute and
776 State University, Blacksburg, VA.

- 777 Cibin, G., Mottana, A., Marcelli, A., and Brigati, M.F. (2006) Angular dependence of potassium
778 K-edge XANES spectra of trioctahedral micas: Significance for the determination of the
779 local structure and electronic behavior of the interlayer site. *American Mineralogist*, 91,
780 1150-1162.
- 781 Cibin, G., Mottana, A., Marcelli, A., Cinque, G., Xu, W., Wu, Z., and Brigatti, M.F. (2010) The
782 interlayer structure of trioctahedral lithian micas: An AXANES spectroscopy study at the
783 potassium K-edge. *American Mineralogist*, 95, 1084-1094.
- 784 Clegg, S.M., Skulte, E., Dyar, M.D., Barefield, J.E., and Wiens, R.C. (2009) Multivariate
785 analysis of remote laser-induced breakdown spectroscopy spectra using partial least
786 squares, principal component analysis, and related techniques. *Spectrochimica Acta B*,
787 88, 79-88.
- 788 Cottrell, E., Kelley, K.A., Lanzirrotti, A., and Fischer, R.A. (2009) High-precision determination
789 of iron oxidation state in silicate glasses using XANES. *Chemical Geology*, 268, 167-
790 179.
- 791 Debret, B., Andreani, M., Muñoz, M., Bolfan, Casanova, N., Carlut, J., Nicollet, C., Schwartz, S.,
792 and Trcera, N. (2014) Evolution of Fe redox state in serpentine during subduction. *Earth
793 and Planetary Science Letters*, 400, 206-218.
- 794 Delaney, J.S., Dyar, M.D., Sutton, S.R., and Bajt, S. (1996) Redox ratios with relevant
795 resolution: Solving an old problem using the Synchrotron microXANES probe. *Geology*,
796 26, 139-142.
- 797 Delaney, J.S., Dyar, M.D., and Sutton, S.R. (2001) Quantifying X-ray pleochrosim effects in
798 synchrotron micro-XANES microanalyses of elemental oxidation states: feldspar and
799 biotite. *Lunar and Planetary Science*, XXXI, Abstract #1936.

- 800 Dräger, G., Frahm, R., Materlik, G., and Brümmer, O. (1988) On the multiplet character of the
801 X-ray transitions in the pre-edge structure of Fe K absorption spectra. *Physica Status*
802 *Solidi*, 146, 287-294.
- 803 Dyar, M.D., Delaney, J.S., and Sutton, S.R. (2001) Fe XANES spectra of iron-rich micas.
804 *European Journal of Mineralogy*, 13, 1079-1098.
- 805 Dyar, M.D., Gunter, M.E., Delaney J.S., Lanzarotti, A., and Sutton, S.R. (2002b) Use of the
806 spindle stage for orientation of single crystals for microXAS: Isotropy and anisotropy in
807 Fe-XANES spectra. *American Mineralogist*, 87, 1500-1504.
- 808 Dyar, M.D., Gunter, M.E., Delaney, J.S., Lanzarotti, A., and Sutton, S.R. (2002a) Systematics in
809 the structure and XANES spectra of pyroxenes, amphiboles, and micas as derived from
810 oriented single crystals. *Canadian Mineralogist*, 40, 1347-1365.
- 811 Dyar, M.D., Mackwell, S.M., McGuire, A.V., Cross, L.R., and Robertson, J.D. (1993) Crystal
812 chemistry of Fe³⁺ and H⁺ in mantle kaersutites: Implications for mantle metasomatism.
813 *American Mineralogist*, 78, 968-979.
- 814 Dyar, M.D., Breves, E.A., Emerson, E., Bell, S.M., Nelms, M., Ozanne, M.V., Peel, S.E.,
815 Carmosino, M.L., Tucker, J.M., Gunter, M.E., Delaney, J.S., Lanzarotti, A., and
816 Woodland, A.B. (2012) Accurate determination of ferric iron in garnets in bulk
817 Mössbauer spectroscopy and synchrotron micro-XANES. *American Mineralogist*, 97,
818 1726-1740.
- 819 Dyar, M.D., Carmosino, M.L., Tucker, J.M., Brown, E.A., Clegg, S.M., Wiens, R.C., Barefield,
820 J.E., Delaney, J.S., and Ashley, G.M., Driese, S.G. (2012) Remote laser-induced
821 breakdown spectroscopy analysis of East African Rift sedimentary samples under Mars
822 conditions. *Chemical Geology*, 294-295, 135-151.

- 823 Dyar, M.D., McCanta, M., Lanzirotti, A., Sutton, S., Carey, C., Mahadevan, S., and Rutherford,
824 M. (2014) Redox state of iron in lunar glasses using X-ray absorption spectroscopy and
825 multivariate analysis. AGU, Abstract #P12B-01.
- 826 Dyar, M.D., McCanta, M., Breves, E., Carey, C.J., and Lanzirotti, A. (submitted) Accurate
827 predictions of iron redox state in silicate glasses: A multivariate approach. American
828 Mineralogist.
- 829 Erdas, O., Buyukbingol, E., Alpaslan, F.N., Adejare, A. (2010) Modeling and predicting binding
830 affinity of phencyclidine-like compounds using machine learning methods. Journal of
831 Chemometrics, 24, 1-13.
- 832 Evans, K.A., Dyar, M.D., Reddy, S.M., Lanzirotti, A., Adams, D.T., and Tailby, N. (2014)
833 variation in XANES in biotite as a function of orientation, crystal composition, and
834 metamorphic history. American Mineralogist, 99, 443-457.
- 835 Filzmoser, P., Gschwandtner, M., and Todorov, V. (2012) Review of sparse methods in
836 regression and classification with application to chemometrics. Journal of Chemometrics,
837 26, 42-51.
- 838 Forder, S.D., Hannant, O.M., Bingham, P.A., and Hand, R.J. (2009) Concerning the use of
839 standards for identifying coordination environments in glasses. Journal of pPhysics:
840 Conference Series, 217, 012072.
- 841 Galois, L., Calas, G. and Arrio, M.A. (2001) High-resolution XANES spectra of iron in
842 minerals and glasses: structural information from the pre-edge region. Chemical Geology,
843 174, 307-319.

- 844 Giuli, G., Paris, E., Wu, Z., Brigatti, M.F., Cibin, G., Mottana, A., and Marcelli, A. (2001)
845 Experimental and theoretical XANES and EXAFS study of tetra-ferriphlogopite.
846 European Journal of Mineralogy, 13, 1099-1108.
- 847 Giuli, G., Paris, E., Pratesi, G., Koeberl, C., and Cipriani, C. (2003) Iron oxidation state in the
848 Fe-rich layer and silica matrix of Libyan Desert Glass: A high-resolution XANES study.
849 Meteoritics and Planetary Science, 38, 1181-11186.
- 850 Giuli, G., Eeckhout, S.G., Paris, E., Koeberl, C., and Pratesi, G. (2005) Iron oxidation state in
851 impact glass from the K/T boundary at Beloc, Haiti, by high-resolution XANES
852 spectroscopy. Meteoritics and Planetary Science, 40, 1575-1580.
- 853 Grossemy, F., Borg, J., Djouadi, Z., Simionovici, A., Lemelle, L., Eichert, D., Deboffe, D.,
854 Westphal, A.J., and Snead, C.J. (2007) In-site Fe XANES of extraterrestrial grains trapped
855 in aerogel collectors: An analytical test for the interpretation of Stardust sample analyses.
856 Planetary and Space Science, 55, 966-973.
- 857 Gunter, M.E., Belluso, E., and Mottana, A. (2007) Amphiboles: Environmental and health
858 concerns. In Amphiboles: Crystal Chemistry, Occurrences, and Health Concerns,
859 Reviews in Mineralogy and Geochemistry, 67, 453-516.
- 860 Gunter, M.E., Dyar, M.D., Lanzirotti, A., Tucker, J.M., and Speicher, E.A. (2011) Differences
861 in Fe-Redox for asbestiform and nonasbestiform amphiboles from the former vermiculite
862 mine, near Libby, Montana USA. American Mineralogist, 1414-1417.
- 863 Haskell, D. (1999) FLUO: Correcting XANES for self-absorption in fluorescence measurements.
864 <http://www.aps.anl.gov/xfd/people/haskel/fluo.html>.
- 865 Hastie, T., Tibshirani, R., and Friedman, J., 2009. The Elements of Statistical Learning, 2nd Ed.
866 Springer Science, New York, 745 pp.

- 867 Hayes, P.A., Philippa, A., Vahur, S., and Leito, I. (2014) ATR-FTIR spectroscopy and
868 quantitative multivariate analysis of paints and coating materials. *Spectrochimica Acta A*,
869 133, 207-213.
- 870 Hecht, E. (1987) *Optics* (2nd ed.), Addison-Wesley, New York, p. 603.
- 871 Holdaway, M.I., Dutrow, B.L., Borthwick, J., Shore, P., Harmon, R.S., and Hinton, R.W.
872 (1986) H content of staurolite as determined by H extraction line and ion microprobe.
873 *American Mineralogist*, 71, 1135-1141.
- 874 Kalivas, J.H. (1999) Interrelationships of multivariate regression methods using eigenvector
875 basis sets. *Journal of Chemometrics*, 13, 1311-1329.
- 876 Kramchote, S., Nakano, K., Kanlayanarat, S., Ohashi, S., Takizawa, K., and Bai, G. (2014)
877 Rapid determination of cabbage quality using visible and near-infrared spectroscopy.
878 *LWT-Food Science and Technology*, 59, 695-700.
- 879 Lanzirotti, A. (2014) Application of hard X-ray microprobe methods to clay-rich materials. In G.
880 Waychunas (ed.), *CMS Workshop Lecture Series v. 19: Advanced Applications of*
881 *Synchrotron Radiation in Clay Science*, 203-230.
- 882 Lopez-Reyes, G., Sobron, P., Lefebvre, C., and Rull, F. (2014) Multivariate analysis of Raman
883 spectra for the identification of sulfates: Implications for ExoMars. *American*
884 *Mineralogist*, 99, 1570-1579.
- 885 Manceau, A., Chateigner, D. and Gates, W.P. (1998) Polarized EXAFS, distance-valence least
886 squares modeling (DVLS) and quantitative texture analysis approaches to the structural
887 refinements of the Garfield nontronite. *Physics and Chemistry of Minerals*, 25, 347-365.

- 888 Manceau, A., Marcus, M.A., and Tamura, N. (2002) Quantitative speciation of heavy metals in
889 soils and sediments by synchrotron X-ray techniques. *Reviews in Mineralogy and*
890 *Geochemistry*, 49, 341-428.
- 891 Marcus, M.A., Westphal, A.J., and Fakra, S.C. (2008) Classification of Fe-bearing species from
892 K-edge XANES data using two-parameter correlation plots. *Journal of Synchrotron*
893 *Radiation*, 15, 463-468.
- 894 McMaster, W.H., Kerr-Del Grande, N., Mallett, J.H., and Hubbell, J.H. (1969) Compilation of
895 X-ray Cross Sections. Lawrence Radiation Laboratory Report UCRL-50174. National
896 Bureau of Standards.
- 897 Mino, L., Borfecchia, E., Groppo, C., Castelli, D., Martinez-Criado, G., Speiss, R., and Lamberti,
898 C. (2014) Iron oxidation state variations in zoned micro-crystals measured using micro-
899 XANES. *Catalysis Today*, 229, 72-79.
- 900 Morháč, M. (2009) An algorithm for determination of peak regions and baseline elimination in
901 spectroscopic data. *Nuclear Instruments and Methods in Physics Research A*, 600, 478-
902 487.
- 903 Morháč, M., Kliman, J., Matoušek, V., Veselský, M., and Turzo, I. (1997) Background
904 elimination methods for multidimensional coincidence gamma-ray spectra. *Nuclear*
905 *Instruments and Methods in Physics Research A*, 401, 113-132.
- 906 Munoz, M., Vidal, O., Marcaillou, C., Pascarelli, S., Mathon, O., and Farges, F. (2013) Iron
907 oxidation state in phyllosilicate single crystals using Fe-K pre-edge and XANES
908 spectroscopy: Effects of the linear polarization of the synchrotron X-ray beam. *American*
909 *Mineralogist*, 98, 1187-1197.

- 910 Oberti, R., Hawthorne, F.C., Cannillo, E., Cámara, F. (2007) Long-range order in amphiboles. In:
911 Amphiboles: Crystal Chemistry, Occurrence and Health Issues (F.C. Hawthorne, R.
912 Oberti, G. Della Ventura, and A. Mottana eds.). Reviews in Mineralogy and Geochemistry,
913 67, 125-172.
- 914 Oberti, R. (2010) HT behaviour and dehydrogenation processes in monoclinic and orthorhombic
915 amphiboles of petrogenetic relevance. Plinius (a supplement to the European Journal of
916 Mineralogy), 36, 377 (abs).
- 917 Oberti, R., Boiocchi, M., Welch, M.D., and Zema, M. (2013) Towards a model for H T
918 behaviour of (orthorhombic and monoclinic) amphiboles. GAC-MAC Meeting,
919 Winnipeg, Canada, 22-24, Abstracts, 153.
- 920 Oberti, R., Cannillo, E., and Toscani, G. (2012) How to name amphiboles after the IMA2012
921 report: rules of thumb and a new PC program for monoclinic amphiboles.. Periodico di
922 Mineralogia, 81, 257-267.
- 923 Ottolini L, Bottazzi P, Zanetti A, Vannucci R (1995) Determination of hydrogen in silicates by
924 secondary ion mass spectrometry. Analyst 120:1309-1313
- 925 Ottolini L., and Oberti R. (2000) Accurate quantification of H, Li, Be, B, F, Ba, REE, Y, Th, and
926 U in complex matrices: a combined approach based on SIMS and single-crystal structure-
927 refinement. Analytical Chemistry, 72, 16, 3731-3738.
- 928 Pedregosa, F., Varoquaux, G., Gramfort, A., Michel, V., Thirion, B., Grisel, O., Blondel, M.,
929 Prettenhofer, P., Weiss, R., Dubourg, V., Vanderplas, J., Passos, A., Cournapeau, D.,
930 Brucher, M., Perrot, M., Duchesnay, E. (2011) Scikit-learn: Machine learning in Python,
931 Journal of Machine Learning Research, 12, 2825-2830.

- 932 Petit, P.-E., Farges, F., Wilke, M., and Solé, V.A. (2001) Determination of the iron oxidation
933 state in Earth materials using XANES pre-edge information. *Journal of Synchrotron*
934 *Radiation*, 8, 952-954.
- 935 Pettifer, R.F., Brouder, C., Benfatto, M., Natoli, C.R., Hermes, C., and Lopez, M.F.R. (1990)
936 Magic-angle theorem in powder x-ray absorption spectroscopy. *Physical Review B*, 42,
937 37-42.
- 938 Randall, C.R., Shu, L., Chiou, Y.-M., Hagen, K.S., Ito, M., Kitajima, N., Lachicotte, R.J., Zang,
939 Y., and Que, L. (1995) X-ray absorption pre-edge studies of high-spin iron(II)
940 complexes. *Inorganic Chemistry*, 34, 1036-1039.
- 941 Ravel, B. and Newville, M. (2005) ATHENA, ARTEMIS, HEPHAESTUS: data analysis for X-
942 ray absorption spectroscopy using IFEFFIT. *Journal of Synchrotron Radiation*, 12, 537-
943 541.
- 944 Robinson, K., Gibbs, G.V., and Ribbe, P.H. (1971) Quadratic elongation: A quantitative measure
945 of distortion in coordination polyhedra. *Science*, 172, 567-570.
- 946 Schmid, R., Wilke, M., Oberhänsli, R., Janssens, K., Falkenberg, G., Franz, L., and Gaab, A.
947 (2003) Micro-XANES determination of ferric iron and its application in
948 thermobarometry. *Lithos*, 70, 381-390.
- 949 Scordari, F., Dyar, M.D., Schingaro, E., Lacalamita, M., and Ottolini, L. (2010) XRD, micro-
950 XANES, EMPA, and SIMS investigation on phlogopite single crystals from Mt. Vulture
951 (Italy). *American Mineralogist*, 95, 1657-1670.
- 952 Stöhr, J. (1992) NEXAFS spectroscopy (Gomer, R., series Ed., Springer Series in Surface
953 Science, 25.) Springer-Verlag, Berlin. 403 p.

- 954 Wegelin, J.A. (2000) A survey of partial least squares (PLS) methods, with emphasis on the two-
955 block case. Technical report, University of Washington, USA.
- 956 Westre, T.E., Kennepohl, P., DeWitt, J.G., Hedman, B., Hodgson, K.O., and Solomon, E.I.
957 (1997) A multiplet analysis of Fe K-edge 1s-3d pre-edge features of iron complexes. J.
958 Amer. Chem. Soc., 119(27), 6297-6314.
- 959 Wilke, M., Farges, F., Petit, P.-E., Brown, G.E. Jr., and Martin, F. (2001) Oxidation state and
960 coordination of Fe in minerals: An Fe K-XANES spectroscopic study. American
961 Mineralogist, 86, 714-730.
- 962 Zhang, Y.F., Yu, G.Y., Han, L., and Guo, T.T. (2015) Identification of four moth larvae based on
963 near-infrared spectroscopy technology. Spectroscopy Letters, 48, 1-6.
- 964

965

FIGURE CAPTIONS

966 Figure 1. Raw XANES spectra of oriented crystals normalized to incident beam intensity (top).

967 The shape of the post-edge is similar regardless of oxidation state and all spectra have a
968 relatively flat slope. Normalizing these raw spectra to total spectral intensity (dividing each pixel
969 by the sum of all pixels in the spectrum), brings all spectra within 20% in magnitude at 7140 eV,
970 the region of greatest spread (bottom).

971 Figure 2. Pre-processed XANES spectra of oriented crystals covering the entire energy range
972 studied (top) and the pre-edge region (bottom). Intensity variations at 7220 eV in the Full
973 Treatment spectra, for which the post-edge background was modeled with a user-defined
974 polynomial, suggest oscillations continuing beyond 7220 eV. To remediate this, spectra were
975 also edge-step normalized to the average of the last five points in the spectrum in the Minimal
976 Treatment method.

977 Figure 3A. Results of Fe^{3+} predictions based on fits of the energy of the area-normalized pre-
978 edge centroid vs. Fe^{3+} measured by Mössbauer. Best-fit lines are shown with long dashes in red;
979 1:1 lines are shown as green dotted lines. Error bars are $\pm 3\%$ on the x axis (the maximum error
980 associated with Mössbauer $\% \text{Fe}^{3+}$ measurements) and $\pm \text{RMSEP}$ from Table 4 for the y axis.

981 Figure 3B. Results of Fe^{3+} predictions based on fits of the energy of the area-normalized pre-
982 edge centroid vs. Fe^{3+} measured by Mössbauer. Best-fit lines are shown with long dashes in red;
983 1:1 lines are shown as green dotted lines. Error bars are $\pm 3\%$ on the x axis (the maximum error
984 associated with Mössbauer $\% \text{Fe}^{3+}$ measurements) and $\pm \text{RMSEP}$ from Table 4 for the y axis.

985 Figure 4. Extracted pre-edges from oriented crystals along with crystal structure diagrams of the
986 M[1]-M[3] sites in each crystal (M[1] at left, M[2] in center column, M[3] at right), viewed

987 down the corresponding axis. The range of the y axis scale is the same for all three orientations
988 of each individual crystal, but note that the y axis maximum is different for each sample based on
989 characteristics of that particular composition. Fitted peaks are color-coded with red as lowest
990 energy, green as middle, and blue as highest energy peak.

991 Figure 5. Predicted vs. “true” Mössbauer %Fe³⁺ values for randomly-oriented crystals of
992 amphibole from this study using models analogous to those described by Berry et al. (2010).
993 (left) Predictor was pre-edge energy at edge intensity of 0.38 for minimal treatment, edge
994 intensity of 0.31 for full treatment. (center) Predictor was intensity at 7111.70/7112.80 eV for
995 minimal treatment and 7111.70/7112.70 eV for full treatment (right) Predictor was first
996 derivative at 7119.00 eV for minimal treatment and 7112.4 eV for full treatment. For each of
997 these models, we regressed against every possible predictor and chose the predictor with highest
998 R² with %Fe³⁺.

999 Figure 6. PLS coefficients and loadings for full treatment spectra. Models used here tuned the
1000 hyperparameter, q , differently for each model using the global minimum number of components
1001 among the first ten. On each pair of plots, intensity is plotted in blue relative to the left axis and
1002 the PLS loadings (top of each pair) and coefficients (bottom of each pair) are plotted in red
1003 dashed lines relative to the right vertical axes.

1004 Figure 7. Locations and magnitudes of lasso coefficients in the full treatment models. On each
1005 plot, the left axis in blue is intensity, and the right axis shows the magnitude of the lasso
1006 coefficients, which are indicated as red lines ending in circles. When compared to Figure 5, it is
1007 apparent that the lasso models use many fewer channels (as few as five); moreover, such sparser
1008 models are also considered to be more generalizable.

1009 Figure 8. Comparison of lasso coefficients for the full-treatment and minimal-treatment models.
1010 Only one coefficient does not fall in these energy ranges: in the X from X model (only), channel
1011 7137 eV has a coefficient of 117. An average XANES spectrum of the amphiboles is shown as
1012 dashed magenta lines for reference. The chosen channels are very similar but not identical due to
1013 a slight offset introduced by the over-absorption correction.

1014 Figure 9. Full treatment PLS and lasso models run using all data to predict all data, with input as
1015 first derivatives of the spectra rather than raw spectral intensity.

1016 Figure 10. Visible Spectra of two amphiboles from the Mineral Spectroscopy Server at Caltech
1017 (<http://minerals.gps.caltech.edu/>). Pargasite is from Oxbrow, NJ, plotted as 1.00 mm thick, while
1018 kaersutite is GRR #1029, plotted for 0.05 mm. The kaersutite spectrum is dominated by
1019 intervalence charge transfer bands, but the pargasite shows characteristic features arising from
1020 Fe²⁺ in M[4] (~1,000 nm, or 10,000 cm⁻¹) and M[1] and M[3] (1400 nm, or 7,100 cm⁻¹). The
1021 M[1]- M[3] site band is strongest in the alpha orientation perpendicular to the plane of the I-
1022 beams. The asymmetric M[4] site band is most intense in the beta direction across the I-beams.

1023 Figure 11. Normalized total pre-edge area plotted against the site distortion parameters angular
1024 variance, σ (left y axis) and quadratic elongation λ (right y axis, solid symbols). Error bars on
1025 these parameters are estimated to be ± 0.001 for total pre-edge area, $\pm 1^\circ$ for σ , and ± 0.001 for λ .
1026 These data indicate that overall pre-edge intensity is poorly correlated with site distortion as
1027 measured by these parameters.

1028 Figure 12. View down the x axis of the amphibole structure, with tetrahedral chains removed
1029 (top) and superimposed (bottom), showing how the M[3] site is surrounded by M[1] and M[2].
1030 The geometry of the M[3] site is strongly affected by the dimension/conformation of the other

1031 octahedra, in particular of M[1], where most of the oxidation related to deprotonation occurs.

1032 This arrangement may explain the trend in Figure 10 showing that the relationship between pre-
1033 edge area and site geometry is most apparent for the M[3] site.

1034 Figure 13. Summary diagram comparing root mean squared prediction errors associated with
1035 minimal (top) and full treatment (bottom) models. Shown are prediction errors for methods listed
1036 as Linear Edge, which uses the energy of the main absorption edge at the location where the
1037 normalized edge intensity has the highest R^2 correlation with $Fe^{3+}/\Sigma Fe$; Linear Ratio, which uses
1038 pre-edge energy at edge intensity of 0.38 for minimal treatment, edge intensity of 0.31 for full
1039 treatment; Linear Slope, which uses of the first derivative at every channel to select the best
1040 predictor channel; partial least-squares models on data and their first derivatives; and least
1041 absolute shrinkage and selection operator models (Lasso) results from data and their first
1042 derivatives.

1043 Figure 14. Comparison of PLS and lasso models for garnet data (left) from Dyar et al. (2012)
1044 against PLS and lasso results from this study for amphibole (right). Error bars in the direction of
1045 the x axis on all plots are $\pm 1-3\%$ absolute for Mossbauer data corrected for recoil-free fraction.
1046 The amphibole predictions are slightly less accurate than those for garnet because amphiboles
1047 are not isometric and thus display different spectra along the X, Y, and Z optical orientation
1048 directions.

1049 Figure 15. PLS loadings and coefficients and lasso coefficients for garnet models from Figure
1050 12. As for amphibole, the predominance of information about Fe valence state is in the main-
1051 edge and EXAFS region indicated by the dashed lines for PLS and the vertical lines for the lasso.

Table 1. Selected previous mineral and glass studies quantifying Fe³⁺/ΣFe using XANES

Material	Method and part of spectrum used for quantification, notes	Citation
silicate glasses, minerals	Changes in amplitude of Fe ²⁺ and Fe ³⁺ Lorentzian peaks fit to pre-edge	Calas and Petiau (1983a)
pyrite, hematite, siderite, Fe metal	Observed orientation dependence for non-cubic minerals and varying magnitudes of pre-edge features	Dräger et al. (1988)
hematite, magnetite, and olivine	Universal calibration line based on pre-edge centroid area and hematite, magnetite, and olivine standards to predict Fe ²⁺ and Fe ³⁺	Bajt et al. (1994)
almandine, fayalite, staurolite, aegirine, leucite, orthoclase	Pre-edge peak heights of model compounds	Henderson et al. (1995)
model compounds	Pre-edge intensities of 50 Fe complexes to assess pre-edge features as a function of symmetry and coordination	Westre et al. (1997)
olivine, pyroxene, amphibole, mica, tourmaline	Centroids of area-normalized pre-edge peaks for mineral groups shown to be distinct, requiring difference calibrations for each group	Delaney et al. (1998)
biotite, nontronite	Pre-edge peak position of oxidized vs. reduced samples	Manceau et al. (2000)
silicate glasses	Components fit to pre-edge used to create calibration curve	Bonnin-Masbah et al. (2001)
biotite	Created calibration for mica Fe ³⁺ /ΣFe using pre-edge features	Dyar et al. (2001)
8 grandierites and some model compounds	Peak-area normalized pre-edge centroids of ⁵⁵ Fe ²⁺ are affected by substitution of ¹⁶ Fe ³⁺ so Wilke et al. (2001) calibration standards must be carefully selected	Farges (2001)
mineral standards	Linear combination of fits to Fe ³⁺ and Fe ²⁺ peaks in pre-edge of standards used to identify valence state and coordination number in glasses	Galoisy et al. (2001)
35 minerals and synthetic compounds	Position of peak-area normalized pre-edge centroid varies by 1.4±0.1 eV for Fe ²⁺ and Fe ³⁺	Petit et al. (2001)
30 minerals and synthetic compounds	Position of peak-area normalized pre-edge modeled with ≤3 pseudo-Voigt lineshapes to predict Fe ²⁺ and Fe ³⁺ with ±10mol% accuracy	Wilke et al. (2001)
enstatite, augite, aegirine, kaersutite, annite, phlogopite	Centroids of pre-edge spectra acquired along X, Y, Z optical orientations vary greatly, resulting in ±20% in Fe ³⁺ /ΣFe for pyroxenes and amphiboles and ±10-15% for micas	Dyar et al. (2002a)
almandine, buergerite, scapolite, fayalite	Centroids of pre-edge spectra acquired along X, Y, Z optical orientation show no variation for isotropic garnet but considerable shift for uniaxial minerals	Dyar et al. (2002b)
orthopyroxenes	Non-linear changes in main Fe K-edge with composition, no change in Fe ³⁺ /ΣFe	Giuli et al. (2002)
obsidian, magnetite, FeO	Used main edge position to infer Fe ³⁺ contents	Lytle and Pingitore (2002)
silicate glasses	Position of peak-area normalized pre-edge used	Wilke et al. (2002)
silicate glasses, fayalite, hematite, magnetite	Determined using linear combinations of end-member pre-edge spectra with 0% and 100% Fe ³⁺ . Found that mineral standards were poor predictors of Fe ³⁺ /ΣFe but glass standards worked well.	Berry et al. (2003)
Libyan desert glass	Used pre-edge spectra of mineral standards to predict Fe ³⁺ /ΣFe in silicate glasses along with fits to pseudo-Voigt functions following Wilke et al. (2001)	Giuli et al. (2003)
eclogite minerals	Applied Wilke et al. (2001) pre-edge calibration to predict Fe ³⁺ /ΣFe in thin sections; used rotation test.	Schmid et al. (2003)
silicate glass	Used pre-edges of 27 silicate glasses; showed no change in CN with oxidation for constant composition	Farges et al. (2004)
silicate glass	Compared wet chemical, Mössbauer, and XANES pre-edge results	Magnien et al. (2004)
basaltic glass	Compared wet chemical, Mössbauer, and XANES pre-edge results	Wilke et al. (2004, 2005)
impact glass	Applied Giuli et al. (2002) and Wilke et al. (2001) pre-edge calibrations to predict Fe ³⁺ /ΣFe in impact glasses	Giuli et al. (2005)
peralkaline glass	Applied pre-edge data from their own reference glasses and Wilke et al. (2001) calibration	Métrich et al. (2006)
silicate glass	Applied Berry et al. (2003) calibration and intensity-weighted pre-edge energy	O'Neill et al. (2006)
silicate glass	Applied Wilke et al. (2001) pre-edge calibration to predict Fe ³⁺ /ΣFe in thin sections	Wilke et al. (2006)
Stardust extraterrestrial grains	Used intensity-weighted average of pre-edge components and Wilke et al. (2001) methods	Grossemey et al. (2007)

silicate glass	Studied pre-edges and EXAFS of glasses to understand Fe coordination	Wilke et al. (2007)
komatiites	Compared pre-edge data of unknowns to their own MORB reference glasses	Berry et al. (2008)
impact glass	Applied Wilke et al. (2001) pre-edge calibrations to predict $\text{Fe}^{3+}/\Sigma\text{Fe}$ and Fe coordination in impact glasses	Giuli et al. (2008)
oxide and silicate glasses	Matched glass XAS spectra against powdered oxide standards to identify oxides and Wilke methods	Hurai et al. (2008)
iron-phosphate glasses	Assessed Fe^{3+} contents in powdered samples using FeO , Fe_2O_3 , Fe_3O_4 , and $\text{Fe}_2(\text{SO})_4$ standards	Qiu et al. (2008)
nuclear waste glass	Used Magnien et al. (2004) glass calibration based on pre-edge	Cochain et al. (2009)
silicate glasses	Compared pre-edge data of unknowns to their own reference glasses to create reference glasses	Cottrell et al. (2009)
minerals and glasses	Compared pre-edge data on mixed-valence reference glass standards	Forder et al. (2009)
silicate glasses	Compared pre-edge data of unknowns to their own reference glasses to create reference glasses	Kelley and Cottrell (2009)
LAP04840 chondrite	Compared pre-edge spectra from single crystal amphiboles to spectra from their own amphibole standards	Ota et al. (2009)
garnet	Compared pre-edge and main-edge data on garnet standards to develop calibration	Berry et al. (2010)
vivianite	Used Fityk program to fit pre-edge and derive valence information	Figueiredo et al. (2010)
phlogopite	Used Bajt et al. (1994) pre-edge calibration, different orientations of crystals, compared against Mössbauer	Scordari et al. (2010)
phonolite glass	Used pre-edge spectra of mineral standards to predict $\text{Fe}^{3+}/\Sigma\text{Fe}$ in silicate glasses along with fits to pseudo-Voigt functions following Wilke et al. (2001)	Giuli et al. (2011)
CI, CM chondrites	Applied Wilke et al. (2001) pre-edge calibrations and in-house powdered mineral standards	Beck et al. (2012)
garnet	Used Berry et al. (2010) pre-edge and main-edge data from garnet standards for calibration	Borfecchia et al. (2012)
garnet	Used multivariate analysis of pre-edge and main-edge data from in-house garnet standards for calibration	Dyar et al. (2012)
rhyolitic glass	Used pre-edge spectra of powdered mineral standards to predict $\text{Fe}^{3+}/\Sigma\text{Fe}$ in silicate glasses along with fits to pseudo-Voigt functions following Wilke et al. (2001)	Giuli et al. (2012)
basaltic glass	Used Cottrell et al. (2009) pre-edge glass calibration	Kelley and Cottrell (2012)
serpentine	Applied Wilke et al. (2001) pre-edge calibrations	Andreani et al. (2013)
garnet	Used Berry et al. (2010) pre-edge and main-edge data from garnet standards for calibration	Berry et al. (2013)
soda-lime silicate glass	Applied Wilke et al. (2001) pre-edge calibrations, showed that low-iron glasses can be photoreduced	Gonçalves Ferreira et al. (2013)
silicate glass	Used pre-edge peak position to confirm lack of Fe^{2+}	Bingham et al. (2014)
amphibole	Applied Wilke et al. (2001) pre-edge calibrations to study of amphibole powders	Bonadiman et al. (2014)
serpentine	Applied Wilke et al. (2001) pre-edge calibrations	Debret et al. (2014)
biotite	Used Dyar et al. (2001) pre-edge calibration based on micas	Evans et al. (2014)
naxhlites	Fitted components to pre-edge and used method similar to Wilke et al. (2001) and Berry et al. (2003)	Hicks et al. (2014)
garnet, omphacite	Used pre-edge positions in almandine, augite, aegirine standards as references, noted orientation effects	Mino et al. (2014)
shergottites	Ratioed Fe^{3+} to Fe^{2+} components in pre-edge	Satake et al. (2014)

Table 2. Samples studied

Sample code	Species*	Locality	Reference
84-BM	magnesio-hastingsite	Dreiser Weiher, Germany, Brück-Raders cone, cognate	Dyar et al. (1993)
86-BM	pargasite	Bullenmerri maar, Victoria, Australia	Dyar et al. (1993)
AK-M2	pargasite	Harrat al Kishb, Saudi Arabia, Coleman locality H271	Dyar et al. (1993)
DL-5	kaersutite	Deadman Lake, California, Hill 2237	Dyar et al. (1993); Oberti et al. (2012)
DL-5 HT	kaersutite	Deadman Lake, California, Hill 2237	Oberti et al. (2012)
DL-7	ferri-kaersutite	Deadman Lake, California, Hill 2237	Dyar et al. (1993)
FA-861	pargasite	Grenville Orogen, Ontario	Cosca et al. (1991)
Fr-11	ferri-kaersutite	Massif Central, France, just east of Alleyras basalt flow	Dyar et al. (1993)
Fr-12	ferri-kaersutite	Massif Central, France, Montgros, from oxidized vent agglomerate	Dyar et al. (1993); Oberti et al. (2012)
Fr-12 HT	ferri-kaersutite	As above, except heat-treated	Oberti et al. (2012)
Kakanui	Ti-rich pargasite	Kakanui, New Zealand, USNM 109647/50	Dyar et al. (1993)
KAR	potassic-pargasite	Old Orefield, Pitkaranta, Karelia, Russia	Oberti et al. (2012)
KAR HT	"oxo-potassic-pargasite"	As above, except heat-treated	Oberti et al. (2012)
MIN-864	magnesio-hornblende	Grenville Orogen, Ontario	Cosca et al. (1991)
PBM1B	tremolite	O'Neill Iron Mine, Sterling New Jersey	This study
PBM2	pargasite	Location 2 Edenville (Warwick Town) NY	This study
PBM5	pargasite	Warwick Location 5 Adams Property, Mountainside x Big Island Rds, Edenville, NY	This study
PBM6	ferri-edenite	Warwick Location 6 PMB 15A pty, Swale with scapolite rock, pegmatite (ridge), FM (lower part)	This study
Tm	kaersutite	Easy Chair Crater, Lunar Crater, Nevada	Dyar et al. (1993)
Z2124	pargasite	Zabargad island, Red Sea	Piccardo et al. (1993), Oberti et al. (2012)
Z2124-HT	"oxo-pargasite"	As above, except heat-treated	Oberti et al. (2012)

* Amphibole names are given according to Hawthorne et al. (2012). Names between "" refer to heat-treated samples.

Table 3. Sample compositions and crystal-chemical formulas*

	84-BR	86-BM	AK-M2	DL-5 SREF	DL-5-HT SREF	DL-7	FA861	Fr-11	Fr-12 SREF	Fr-12-HT SREF	Kakanui
Oriented?	random	random	both	oriented	oriented	random	random	random	oriented	oriented	random
SiO ₂	39.29	41.91	39.93	39.62	39.62	39.85	40.94	40.05	39.56	39.56	39.32
Al ₂ O ₃	13.85	14.46	14.83	13.54	13.54	14.39	13.28	14.48	13.8	13.8	13.54
TiO ₂	3.27	3.23	5.31	4.64	4.64	4.51	2.69	4.49	5.15	5.15	4.89
FeO _T	10.51	7.97	11.04	11.80	11.80	13.90	15.97	12.88	10.46	10.46	11.02
Cr ₂ O ₃	0.02	0.77	0.02	0.01	0.01	0.00	0.00	0.02	0.03	0.03	0.00
MgO	13.77	15.16	12.84	11.61	11.61	11.26	10.01	11.92	12.71	12.71	12.31
MnO	0.10	0.11	0.09	0.13	0.13	0.20	0.27	0.09	0.10	0.10	0.14
ZnO	n.a.	n.a.	n.a.	0.10	0.10	n.a.	n.a.	n.a.	0.03	0.03	n.a.
NiO	n.a.	n.a.	n.a.	0.01	0.01	n.a.	n.a.	n.a.	0.03	0.03	n.a.
CaO	12.10	10.74	9.87	10.87	10.87	10.82	10.57	10.73	11.27	11.27	9.96
Na ₂ O	1.96	3.18	2.91	2.35	2.35	2.74	3.12	2.73	2.33	2.33	2.56
K ₂ O	2.18	1.21	1.10	1.64	1.64	1.50	1.04	1.35	1.48	1.48	2.06
F	0.00	0.00	0.00	0.14	0.14	0.20	0.05	0.00	0.09	0.09	0.18
Cl	0.00	0.00	0.00	0.01	0.01	0.02	0.46	0.00	0.03	0.03	0.02
H ₂ O	1.41	1.13	1.03	0.86	0.00	0.90	1.43	0.48	0.07	0.02	1.14
- O=F	-	-	-	0.06	0.06	0.08	0.02	-	0.04	0.04	0.08
- O=Cl	-	-	-	0.00	0.00	0.00	0.10	-	0.01	0.01	0.00
Sum	98.37	99.87	98.97	97.07	96.40	100.29	102.71	99.22	97.07	97.02	97.06
Mössbauer %Fe ³⁺ †	44	23	25	34	89	41	18	72	72	100	28
Si	5.874	6.066	5.944	6.051	6.051	5.922	5.985	5.945	5.972	5.972	5.990
Al	2.126	1.934	2.056	1.949	1.949	2.078	2.015	2.055	2.028	2.028	2.010
Σ T cations	8.000	8.000	8.000	8.000	8.000	8.000	8.000	8.000	8.000	8.000	8.000
Al	0.315	0.533	0.547	0.489	0.489	0.443	0.481	0.479	0.428	0.428	0.422
Fe ³⁺	0.582	0.230	0.344	0.666	1.348	0.699	0.346	1.158	1.274	1.321	0.414
Ti	0.368	0.352	0.594	0.533	0.533	0.504	0.494	0.501	0.585	0.585	0.560
Cr	0.002	0.088	0.002	0.001	0.001	0.011	0.000	0.002	0.004	0.004	0.000
Zn	-	-	-	0.011	0.011	-	-	-	0.003	0.003	-
Ni	-	-	-	0.000	0.000	-	-	-	0.000	0.000	-
Mg	3.066	3.268	2.847	2.641	2.618	2.492	2.180	2.635	2.706	2.659	2.793
Fe ²⁺	0.667	0.529	0.666	0.659	0.000	0.851	1.499	0.211	0.000	0.000	0.811
Mn ²⁺	0.000	0.000	0.000	0.000	0.000	0.000	0.000	0.000	0.000	0.000	0.000
Σ C cations	5.000	5.000	5.000	5.000	5.000	5.000	5.000	5.000	5.000	5.000	5.000
Mg	0.000	0.000	0.000	0.000	0.023	0.000	0.000	0.000	0.152	0.199	0.000
Fe ²⁺	0.065	0.206	0.365	0.182	0.159	0.178	0.108	0.230	0.047	0.000	0.179
Mn	0.013	0.013	0.011	0.017	0.017	0.025	0.033	0.011	0.013	0.013	0.018
Ca	1.922	1.666	1.574	1.779	1.779	1.723	1.656	1.707	1.788	1.788	1.626
Na	0.000	0.115	0.050	0.022	0.022	0.074	0.203	0.052	0.000	0.000	0.177
Σ B cations	2.000	2.000	2.000	2.000	2.000	2.000	2.000	2.000	2.000	2.000	2.000
Ca	0.016	0.000	0.000	0.000	0.000	0.000	0.000	0.000	0.035	0.035	0.000
Na	0.568	0.777	0.790	0.674	0.674	0.715	0.681	0.734	0.682	0.682	0.579
K	0.416	0.223	0.209	0.320	0.320	0.284	0.194	0.256	0.285	0.285	0.400
Σ A cations	1.000	1.000	0.999	0.994	0.994	0.999	0.875	0.990	1.002	1.002	0.979
OH	1.476	1.496	1.023	0.682	0.000	0.892	1.394	0.475	0.070	0.020	1.158
F	0.000	0.000	0.000	0.068	0.068	0.094	0.023	0.000	0.043	0.043	0.087
Cl	0.000	0.000	0.000	0.003	0.003	0.005	0.114	0.000	0.008	0.008	0.005
O	0.524	0.504	0.977	1.247	1.929	1.009	0.469	1.525	1.879	1.929	0.750
Σ W anions	2.000	2.000	2.000	2.000	2.000	2.000	2.000	2.000	2.000	2.000	2.000
Calc. %Fe ³⁺	44	24	25	44	89	41	18	72	96	100	29

*Formulas calculated based on 24 (O,Cl,F) apfu and 2 (O,OH,Cl,F) apfu and taking into account the Fe³⁺/Fe²⁺ ratio obtained from Mössbauer or SREF analysis; n.a. = not analyzed.

†%Fe³⁺ calculated from Mössbauer peak areas and then corrected for differential recoil-free fraction as described in Dyar et al. (1993).

Table 3, continued. Sample Compositions and crystal-chemical formulas *

	KAR SREF	KAR-HT SREF	MIN864	PBM1B	PBM2	PBM5	PBM6	Tm	Z2124 SREF	Z2124-HT SREF
Oriented?	oriented	oriented	random	random	random	random	random	both	oriented	oriented
SiO ₂	39.54	39.54	44.53	57.53	43.42	40.48	47.95	39.52	47.48	47.48
Al ₂ O ₃	0.79	15.47	10.15	0.67	10.40	14.68	8.19	14.03	9.56	9.56
TiO ₂	15.47	0.79	0.91	0.00	1.13	0.32	0.32	5.87	0.34	0.34
FeO _T	0.01	14.78	16.81	4.38	13.50	10.32	2.38	12.22	4.65	4.65
Cr ₂ O ₃	14.78	0.01	0.00	0.00	0.00	0.01	0.03	0.00	1.38	1.38
MgO	0.59	10.31	10.40	21.75	12.70	12.93	21.81	11.71	19.48	19.48
MnO	0.00	0.59	0.33	0.06	0.24	0.38	0.05	0.17	0.02	0.02
ZnO	0.00	0.00	n.a	n.a	n.a	n.a	n.a	n.a	0.00	0.00
NiO	0.00	0.00	n.a	n.a	n.a	n.a	n.a	n.a	0.00	0.00
CaO	10.31	12.03	11.59	13.26	11.63	11.96	12.39	11.10	10.49	10.49
Na ₂ O	12.03	1.30	1.48	0.24	2.82	2.31	2.72	2.81	3.77	3.77
K ₂ O	1.30	2.64	1.21	0.15	1.05	1.79	0.65	1.29	0.56	0.56
F	2.64	1.30	0.15	1.29	2.30	2.01	2.39	0.00	0.10	0.10
Cl	1.20	0.00	0.08	0.03	0.16	0.33	0.09	0.00	0.00	0.00
H ₂ O	1.30	0.00	1.55	1.35	0.70	1.04	0.95	0.27	2.00	1.52
- O=F	0.55	0.55	0.08	0.54	0.97	0.85	1.01	-	0.10	0.10
- O=Cl	0.00	0.00	0.06	0.01	0.04	0.07	0.02	-	0.00	0.00
Sum	99.41	99.51	99.10	99.93	99.05	97.64	98.89	98.99	99.79	99.31
Mössbauer %Fe ³⁺ †	28	100	33	26	18	15	4	77	36	100
Si	5.934	5.934	6.655	7.934	6.501	6.095	6.817	5.895	6.729	6.729
Al	2.066	2.066	1.345	0.066	1.499	1.905	1.183	2.105	1.271	1.271
Σ T cations	8.000	8.000	8.000	8.000	8.000	8.000	8.000	8.000	8.000	8.000
Al	0.671	0.671	0.443	0.043	0.337	0.701	0.190	0.362	0.326	0.326
Fe ³⁺	0.651	1.852	0.685	0.130	0.297	0.195	0.012	1.166	0.090	0.551
Ti	0.089	0.089	0.102	0.000	0.127	0.036	0.034	0.658	0.036	0.036
Cr	0.001	0.001	0.000	0.000	0.000	0.001	0.003	0.000	0.155	0.155
Zn	0.000	0.000	-	-	-	-	-	-	0.000	0.000
Ni	0.000	0.000	-	-	-	-	-	-	0.000	0.000
Mg	2.305	2.305	2.315	4.468	2.832	2.900	4.618	2.602	4.112	4.112
Fe ²⁺	1.205	0.004	1.417	0.359	1.393	1.105	0.143	0.212	0.281	0.000
Mn ²⁺	0.075	0.075	0.038	0.000	0.014	0.048	0.000	0.000	0.000	0.000
Σ C cations	4.997	4.997	5.000	5.000	5.000	4.986	5.000	5.000	5.000	5.000
Mg	0.000	0.000	0.000	0.000	0.000	0.000	0.000	0.000	0.000	0.180
Fe ²⁺	0.000	0.000	0.000	0.016	0.000	0.000	0.128	0.146	0.180	0.000
Mn	0.000	0.000	0.004	0.007	0.016	0.000	0.006	0.021	0.002	0.002
Ca	1.935	1.935	1.856	1.960	1.866	1.930	1.866	1.774	1.593	1.593
Na	0.065	0.065	0.140	0.017	0.118	0.070	0.000	0.059	0.255	0.255
Σ B cations	2.000	2.000	2.000	2.000	2.000	2.000	2.000	2.000	2.000	2.000
Ca	0.000	0.000	0.000	0.000	0.000	0.000	0.022	0.000	0.000	0.000
Na	0.313	0.313	0.289	0.047	0.701	0.604	0.750	0.754	0.811	0.811
K	0.505	0.505	0.231	0.026	0.201	0.344	0.118	0.245	0.101	0.101
Σ A cations	0.818	0.818	0.520	0.073	0.902	0.948	0.890	0.999	0.912	0.912
OH	1.201	0.000	1.540	1.269	0.699	1.044	0.901	0.318	1.890	1.437
F	0.617	0.617	0.071	0.563	1.089	0.957	1.075	0.000	0.045	0.045
Cl	0.000	0.000	0.020	0.007	0.041	0.084	0.022	0.000	0.000	0.000
O	0.182	1.383	0.369	0.161	0.171	0.000	0.002	1.682	0.065	0.518
Σ W anions	2.000	2.000	2.000	2.000	2.000	2.085	2.000	2.000	2.000	2.000
Calc. %Fe ³⁺	35	100	33	26	18	15	4	77	36	100

*Formulas calculated based on 24 (O,Cl,F) apfu and 2 (O,OH,Cl,F) apfu and taking into account the Fe³⁺/Fe²⁺ ratio obtained from Mössbauer or SREF analysis; n.a.= not analyzed. †%Fe³⁺ calculated from Mössbauer peak areas and then corrected for differential recoil-free fraction as described in Dyar et al. (1993).

Table 4. Parameters of pre-edge fits using full treatment models

	MS %Fe ³⁺	Area	Centroid	FWHM	%Area	Area	Centroid	FWHM	%Area	Area	Centroid	FWHM	%Area	Area	Centroid	FWHM	%Area	χ^2	ANPC
Oriented Crystals																			
DL-5-HT X	89					0.01	7112.57	1.34	13	0.08	7114.16	1.68	87					0.86	7113.95
DL-5-HT Y	89					0.01	7112.47	1.30	15	0.05	7113.99	1.72	85					0.18	7113.76
DL-5-HT Z	89					0.03	7112.65	1.45	48	0.03	7114.08	1.57	52					0.27	7113.39
DL-5 X	32	0.04	7111.63	2.37	49	0.01	7112.94	1.06	8	0.04	7113.94	2.26	43					0.21	7112.74
DL-5 Y	32	0.04	7111.64	2.43	50	0.01	7112.91	1.00	8	0.03	7113.97	2.24	42					0.15	7112.71
DL-5 Z	32	0.03	7111.76	2.39	48	0.00	7113.04	0.88	3	0.03	7114.01	2.51	49					0.08	7112.90
Fr-12-B X	95					0.03	7112.68	1.37	38	0.04	7114.11	1.68	62					0.18	7113.56
Fr-12-B Y	95					0.03	7112.66	1.40	38	0.05	7114.15	1.61	62					0.24	7113.59
Fr-12-B Z	95					0.02	7112.71	1.26	29	0.04	7114.16	1.60	71					0.24	7113.74
PAR-HT X	100					0.04	7112.68	1.38	40	0.05	7114.12	1.71	60					0.57	7113.54
PAR-HT Y	100					0.03	7112.68	1.43	41	0.05	7114.16	1.67	59					0.53	7113.56
PAR-HT Z	100					0.03	7112.74	1.29	44	0.03	7114.17	1.60	56					0.38	7113.54
PAR X	28	0.05	7112.05	2.85	65	0.00	7113.20	0.90	5	0.02	7114.27	1.82	29					0.13	7112.77
PAR Y	28	0.05	7112.08	2.78	62	0.01	7113.16	1.00	7	0.02	7114.30	1.76	31					0.09	7112.85
PAR Z	28	0.02	7111.89	2.21	40	0.00	7112.17	0.50	1	0.03	7113.83	2.25	59					0.12	7113.04
Z2124-HT X	100					0.01	7112.68	1.38	16	0.08	7114.19	1.66	84					0.78	7113.95
Z2124-HT Y	100					0.01	7112.44	1.20	10	0.08	7114.04	1.86	90					0.76	7113.88
Z2124-HT Z	100					0.03	7112.64	1.37	35	0.05	7114.14	1.90	65					0.53	7113.62
Z2124 X	36	0.03	7112.00	2.23	44	0.01	7113.06	1.03	20	0.02	7114.30	1.45	37					0.29	7113.06
Z2124 Y	36	0.05	7112.12	2.35	59	0.01	7112.97	*	10	0.02	7114.30	1.54	30					0.35	7112.87
Z2124 Z	36	0.01	7111.20	1.54	16	0.03	7112.64	1.80	49	0.02	7114.25	1.57	35					0.30	7112.97
AK-M2 X	25	0.07	7112.58	2.93	79	0.00	7113.36	0.66	1	0.02	7114.39	1.62	19					0.17	7112.94
AK-M2 Y	25	0.08	7111.90	2.51	66	0.01	7113.25	1.22	8	0.03	7114.48	1.93	26					0.44	7112.68
AK-M2 Z	25	0.03	7111.64	1.82	48	0.02	7113.06	1.46	29	0.02	7114.38	1.67	23					0.19	7112.68
Fr-12 X	95					0.03	7112.83	1.43	28	0.07	7114.28	1.55	72					0.09	7113.87
Fr-12 Y	95					0.02	7112.86	1.31	32	0.05	7114.27	1.57	68					0.07	7113.82
Fr-12 Z	95					0.02	7112.87	1.30	31	0.05	7114.30	1.51	69					0.08	7113.85
Tm X	77	0.01	7111.50	1.50	13	0.03	7112.84	1.42	40	0.04	7114.29	1.61	47					0.08	7113.36
Tm Y	77	0.01	7111.64	1.50	12	0.02	7112.89	1.35	29	0.04	7114.08	2.07	59					0.08	7113.43
Tm Z	77	0.01	7111.15	1.50	11	0.03	7112.99	1.92	50	0.02	7114.45	1.42	39					0.27	7113.37
Randomly-Oriented																			
Tm	77					0.03	7112.31	2.50	40	0.01	7112.82	1.01	14	0.03	7114.23	1.88	47	0.06	7113.28
PBM-6	4	0.02	7111.26	1.47	31	0.02	7112.56	1.83	23	0.04	7113.97	2.90	46					0.18	7112.81
PBM-5	15	0.03	7111.42	1.70	47	0.00	7112.34	0.63	2	0.01	7113.05	1.35	16	0.03	7113.96	2.63	35	0.18	7112.59
PBM-2	18	0.00	7109.72	1.27	3	0.03	7111.38	1.69	35	0.02	7112.82	1.85	24	0.03	7114.16	3.18	38	0.06	7112.74
PBM-1B	26	0.03	7111.50	1.89	42	0.00	7112.39	0.44	2	0.03	7114.12	2.11	40	0.01	7113.00	1.09	17	0.27	7112.81
MIN-864	38	0.03	7112.00	2.39	51	0.03	7114.36	1.89	41	0.00	7112.37	0.72	2	0.00	7113.20	0.92	6	0.05	7113.04
Kakanui	29	0.02	7111.55	1.82	42	0.02	7113.18	1.71	42	0.00	7114.29	0.96	8	0.00	7115.03	1.15	8	0.08	7112.73
Fr-12	95									0.02	7112.82	1.36	31	0.05	7114.31	1.42	69	0.09	7113.85
Fr-11	66	0.04	7111.83	2.25	44	0.01	7113.06	1.34	17	0.03	7114.33	1.74	35	0.00	7115.79	1.15	4	0.08	7113.05
FA-861	21	0.03	7111.53	1.92	45	0.02	7113.10	1.64	32	0.01	7114.54	1.72	21	0.00	7115.62	0.74	2	0.08	7112.74
DL-7	40	0.03	7112.13	2.42	51	0.01	7114.94	1.30	13	0.01	7113.03	1.10	9	0.02	7114.06	1.53	27	0.05	7113.10
AK-M2	25	0.02	7111.50	1.80	44	0.01	7112.90	1.12	16	0.02	7114.02	1.92	35	0.00	7115.49	1.04	5	0.10	7112.80
86-BM	24	0.06	7112.64	3.26	80	0.01	7114.54	1.36	13	0.00	7111.65	1.51	6	0.00	7113.38	0.64	1	0.11	7112.84
84-BR	43	0.03	7111.81	2.27	36	0.00	7113.08	1.12	6	0.05	7114.00	2.31	58					0.09	7113.16

MS %Fe³⁺ = Percentage of Fe³⁺ as measured by Mössbauer spectroscopy and corrected for recoil-free fraction. Area is in units of normalized intensity. Centroid and FWHM (full width at half peak maximum) are in units of eV, and % area is the relative % of the total pre-edge energy in that peak. χ^2 is the fit of the summed peaks to the data, and ANPC is the area-normalized peak centroid that divides all the spectra area in half.

Table 5. RMSE accuracies and R² values for linear prediction models tested

Treatment	Method	Linear Centroid		Linear Edge		Linear Ratio		Linear Slope	
		RMSE	R ²	RMSE	R ²	RMSE	R ²	RMSE	R ²
Minimal	X from X	n.a.	n.a.	8.9	0.93	9.7	0.92	6.9	0.96
Minimal	Y from Y	n.a.	n.a.	10.3	0.91	14.7	0.81	15.2	0.81
Minimal	Z from Z	n.a.	n.a.	5.0	0.98	5.9	0.97	6.9	0.96
Minimal	X or Y from X and Y	n.a.	n.a.	9.7	0.91	15.2	0.78	20.0	0.68
Minimal	X, Y, or Z from all X, Y, and Z	n.a.	n.a.	10.9	0.89	15.0	0.79	11.9	0.87
Minimal	random from random	n.a.	n.a.	14.5	0.72	14.6	0.73	14.1	0.73
Minimal	random from X, Y, and Z	n.a.	n.a.	15.4	0.69	11.4	0.84	16.2	0.65
Minimal	all from all	n.a.	n.a.	13.8	0.84	11.9	0.88	23.4	0.58
Full	X from X	16.2	0.77	9.1	0.93	5.5	0.97	5.5	0.97
Full	Y from Y	10.4	0.91	12.7	0.87	9.2	0.93	15.0	0.83
Full	Z from Z	13.1	0.85	2.7	0.99	9.3	0.93	2.6	0.99
Full	X or Y from X and Y	13.2	0.84	10.6	0.90	8.2	0.94	19.3	0.70
Full	X, Y, or Z from all X, Y, and Z	12.5	0.85	10.7	0.89	8.6	0.93	17.3	0.72
Full	random from random	13.7	0.76	18.1	0.56	25.4	0.38	13.3	0.76
Full	random from X, Y, and Z	12.2	0.80	14.7	0.72	12.6	0.80	17.1	0.63
Full	all from all	12.5	0.87	12.3	0.87	10.7	0.90	23.9	0.54

n.a. = not analyzed

Table 6. RMSE accuracies and R² values for multivariate prediction models tested

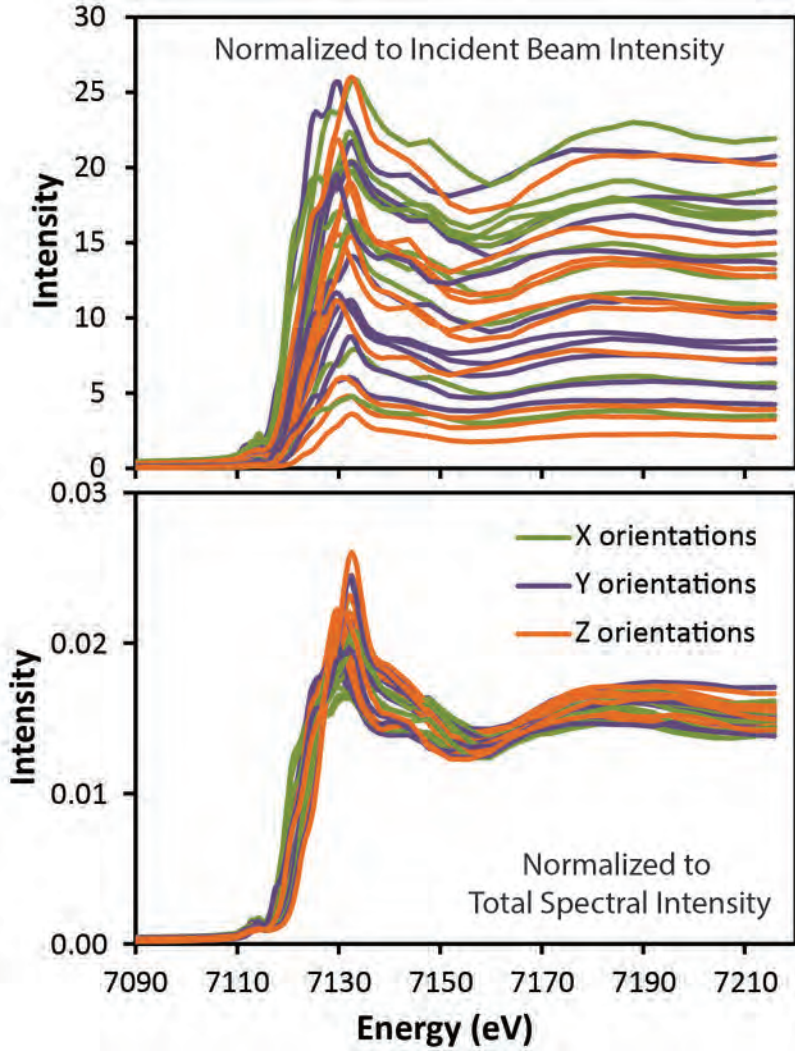
Treatment	Method	Raw Spectra				First Derivative Spectra			
		PLS*		Lasso		PLS*		Lasso	
		RMSE	R ²	RMSE	R ²	RMSE	R ²	RMSE	R ²
Minimal	X from X	1.06	1.00	0.00	1.00	1.06	1.00	0.00	1.00
Minimal	Y from Y	0.24	1.00	7.22	0.95	0.24	1.00	7.22	0.95
Minimal	Z from Z	0.34	1.00	9.26	0.91	0.34	1.00	9.26	0.91
Minimal	X or Y from X and Y	2.67	0.99	6.23	0.96	2.67	0.99	6.24	0.96
Minimal	X, Y, or Z from all X, Y, and Z	3.35	0.99	7.87	0.94	3.36	0.99	7.87	0.94
Minimal	random from random	1.60	0.99	31.15	0.39	1.60	1.00	31.14	0.40
Minimal	random from X, Y, and Z	15.61	0.65	19.42	0.45	15.61	0.64	19.42	0.46
Minimal	all from all	5.48	0.97	9.73	0.92	5.48	0.97	9.74	0.92
Full	X from X	0.36	1.00	0.00	1.00	0.36	1.00	0.00	1.00
Full	Y from Y	0.31	1.00	11.84	0.86	0.31	1.00	11.84	0.86
Full	Z from Z	0.31	1.00	9.69	0.91	0.31	1.00	9.69	0.91
Full	X or Y from X and Y	3.75	0.98	9.32	0.92	3.75	0.99	9.33	0.92
Full	X, Y, or Z from all X, Y, and Z	3.50	0.99	9.89	0.91	3.50	0.99	9.89	0.90
Full	random from random	1.94	0.99	27.85	0.11	1.92	0.99	27.85	0.11
Full	random from X, Y, and Z	13.70	0.73	14.12	0.71	13.70	0.72	14.11	0.71
Full	all from all	6.18	0.97	10.56	0.91	6.17	0.97	10.56	0.90

*PLS models all using 6 components.

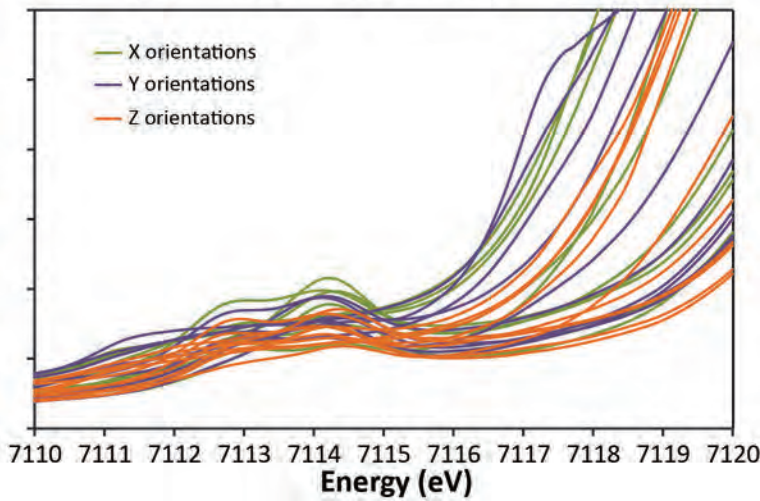
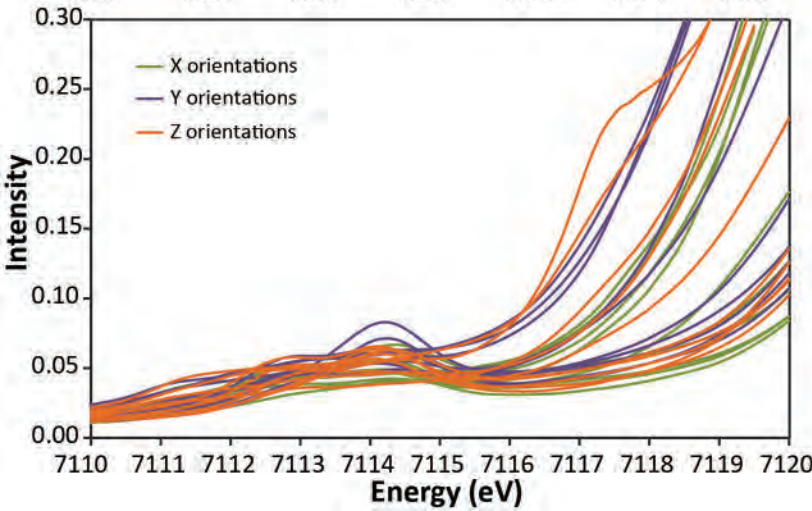
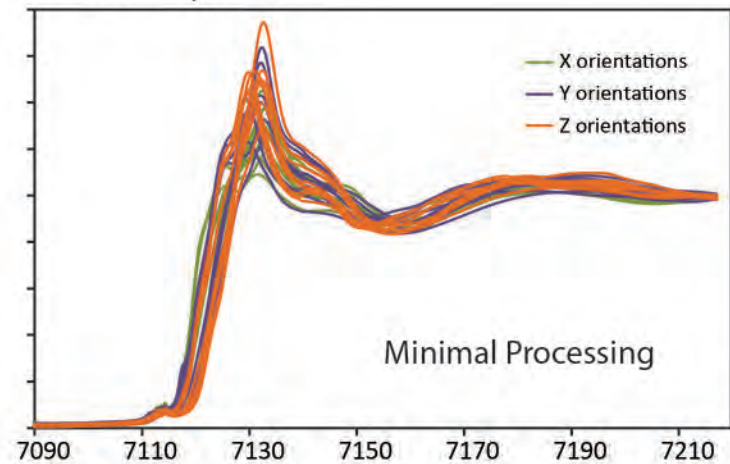
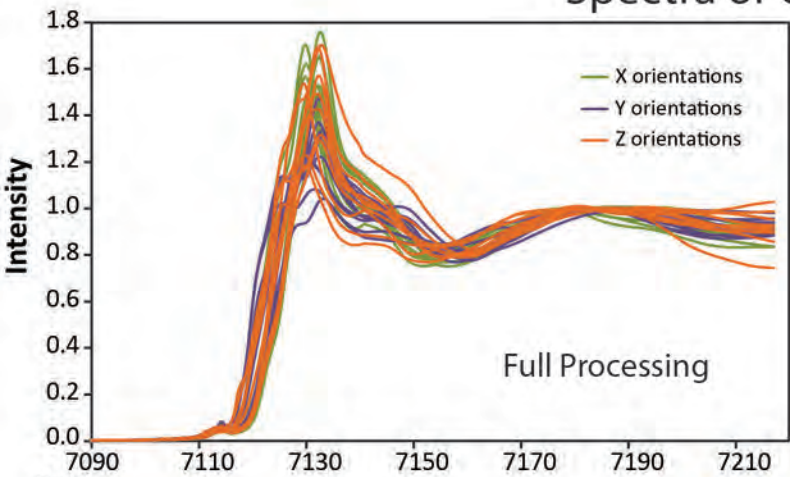
Table 7. Relevant Structure REFinement (SREF) data for selected samples*

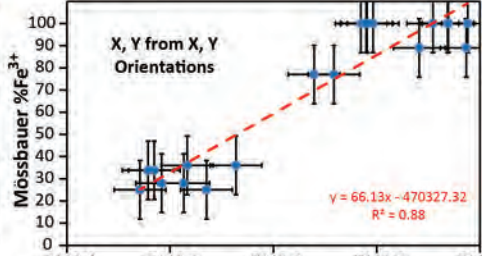
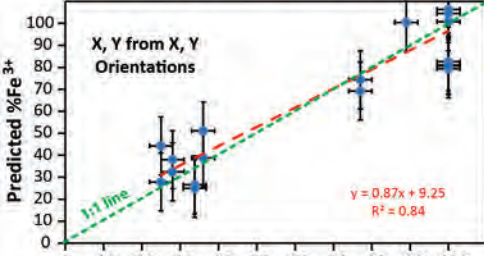
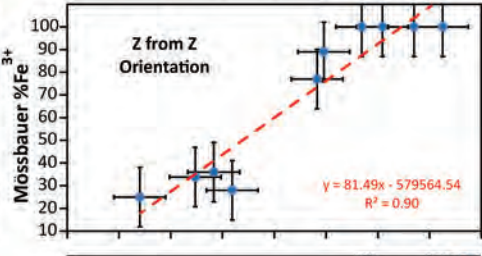
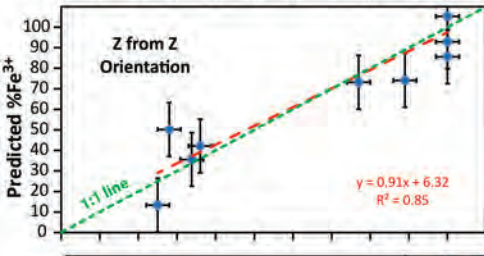
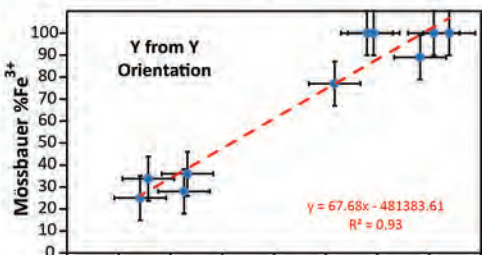
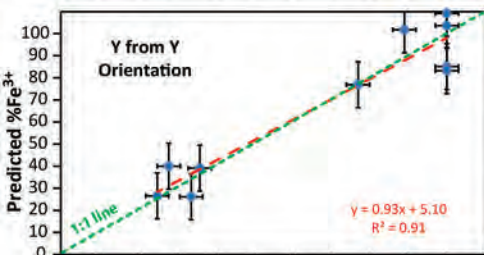
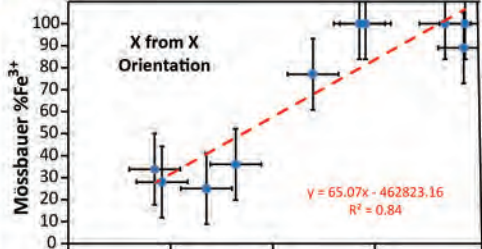
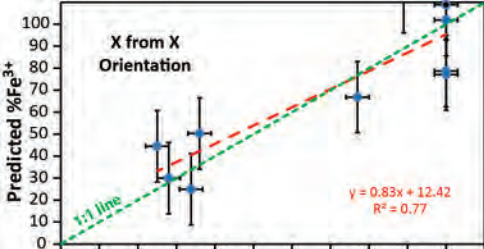
	$M(1) \text{ Fe}^{2+}$	$M(1) \text{ Fe}^{3+}$	$M(2) \text{ Fe}^{2+}$	$M(2) \text{ Fe}^{3+}$	$M(3) \text{ Fe}^{2+}$	$M(3) \text{ Fe}^{3+}$	$M(4) \text{ Fe}^{2+}$
Site populations (atoms per formula unit)							
DL-5	0.50	0.09	0.00	0.43	0.25	0.15	0.10
DL-5-HT	0.16	0.76	0.00	0.19	0.00	0.40	0.00
Fr-12	0.04	0.74	0.00	0.25	0.01	0.28	0.00
Fr-12-HT	0.00	0.78	0.00	0.25	0.00	0.29	0.00
KAR	0.73	0.00	0.02	0.65	0.46	0.00	0.00
KAR-HT	0.00	1.11	0.00	0.46	0.00	0.28	0.00
Z2124	0.11	0.00	0.09	0.09	0.08	0.00	0.18
Z2124-HT	0.00	0.38	0.00	0.08	0.00	0.09	0.00
% of total Fe in each valence state and site							
DL-5	33	6	0	28	17	10	6
DL-5-HT	11	50	0	13	0	26	0
Fr-12	3	56	0	19	1	21	0
Fr-12-HT	0	59	0	19	0	22	0
KAR	39	0	1	35	25	0	0
KAR-HT	0	60	0	25	0	15	0
Z2124	30	0	24	24	22	0	0
Z2124-HT	0	68	0	16	0	16	0
Distortion parameters for the $M(1-3)$ sites							
	$M(1) \lambda^\dagger$	$M(1) \sigma^\dagger$	$M(2) \lambda$	$M(2) \sigma$	$M(3) \lambda$	$M(3) \sigma$	
DL-5	1.0146	45.88	1.0091	27.98	1.0229	72.61	
DL-5-HT	1.0178	53.09	1.0111	34.06	1.0218	68.54	
Fr-12	1.0179	52.82	1.0106	32.37	1.0217	68.33	
Fr-12-HT	1.0172	51.34	1.0108	33.04	1.0211	66.53	
KAR	1.0163	51.23	1.0073	22.71	1.0276	87.09	
KAR-HT	1.0188	58.07	1.0110	34.06	1.0228	70.85	
Z2124	1.0129	41.79	1.0072	22.99	1.0181	58.19	
Z2124-HT	1.0120	38.47	1.0086	26.97	1.0158	51.06	

*Site populations from Oberti et al., in preparation. [†]Site distortion parameters as described in the text.



Spectra of Oriented Crystals





Mossbauer %Fe³⁺

Anorm Centroid (eV)

